© 2018. Published by The Company of Biologists Ltd | Development (2018) 145, dev157487. doi:10.1242/dev.157487

RESEARCH ARTICLE

The non-canonical Wnt-PCP pathway shapes the mouse caudal neural plate

Beatriz López-Escobar[1,*], José Manuel Caro-Vega[1,*], Deepthi S. Vijayraghavan[2], Timothy F. Plageman[3], José A. Sanchez-Alcazar[4], Roberto Carlos Moreno[1], Dawn Savery[5], Javier Márquez-Rivas[6], Lance A. Davidson[2] and Patricia Ybot-González[1,7,‡]

ABSTRACT

The last stage of neural tube (NT) formation involves closure of the caudal neural plate (NP), an embryonic structure formed by neuromesodermal progenitors and newly differentiated cells that becomes incorporated into the NT. Here, we show in mouse that, as cell specification progresses, neuromesodermal progenitors and their progeny undergo significant changes in shape prior to their incorporation into the NT. The caudo-rostral progression towards differentiation is coupled to a gradual reliance on a unique combination of complex mechanisms that drive tissue folding, involving pulses of apical actomyosin contraction and planar polarised cell rearrangements, all of which are regulated by the Wnt-PCP pathway. Indeed, when this pathway is disrupted, either chemically or genetically, the polarisation and morphology of cells within the entire caudal NP is disturbed, producing delays in NT closure. The most severe disruptions of this pathway prevent caudal NT closure and result in spina bifida. In addition, a decrease in *Vangl2* gene dosage also appears to promote more rapid progression towards a neural fate, but not the specification of more neural cells.

KEY WORDS: Caudal neurulation, NMPs, NTDs, Wnt-PCP, Apical contraction, Tissue folding

INTRODUCTION

The organisation and reorganisation of epithelial sheets is a fundamental requirement for reaching developmental milestones such as gastrulation and neural tube (NT) closure, and for events effected by changes in cell shape. Epithelial cells are polarised along their apico-basal axis and are attached tightly to one another by lateral adhesions close to the apical surface of the cell. The tight binding of each epithelial cell to its neighbours means that the apical constriction of several cells will produce a fold in the epithelial sheet. Such apical constriction also occurs to establish epithelial rosettes, which are transient arrangements of five or more epithelial cells around a central point that also contribute to tissue remodelling during development. Apical constriction is produced by contraction of the actomyosin meshwork in the apical domain of these cells, and it is believed to be the driving force for epithelial folding during organogenesis (reviewed by Fletcher et al., 2014; Siedlik and Nelson, 2015; Sutherland, 2016).

Planar cell polarity (PCP) lies perpendicular to the apico-basal axis, and it coordinates morphogenetic cell movements, cell shape and cell migration in an epithelial context, driving cell arrangements in many developing tissues, including the *Drosophila* wing and vertebrate NT (Tada and Kai, 2012; Nikolopoulou et al., 2017; Trichas et al., 2012). PCP is controlled by the Wnt-PCP pathway. The polarised intracellular distribution of Wnt-PCP pathway elements, such as Vangl2, Celsr1 or Shroom3, seems to regulate the cytoskeletal dynamics and apical actomyosin contractility that drives cell movement (Mahaffey et al., 2013; McGreevy et al., 2015; Nishimura et al., 2012; Ossipova et al., 2015). Moreover, homozygous mutations in genes that encode core Wnt-PCP proteins impede the initiation of NT closure (a phenotype known as craniorachischisis) as a result of impairment in convergent extension (CE) movements (Nikolopoulou et al., 2017; Keller, 2002).

In vertebrates, the first evidence of central nervous system (CNS) formation is the thickening of an epiblast region anterior to the primitive streak (PS). Neurulation transforms the neural plate (NP) into a NT, the embryonic precursor of the brain and spinal cord. During the early shaping of the neural ectoderm, the prospective posterior neural cells intercalate along the mediolateral axis through CE movements to form a narrow, long midline. This structure ultimately gives rise to the notochord and the medial hinge point (MHP), the latter facilitating the elevation of the neural folds (Goto and Keller, 2002; Wallingford and Harland, 2002; Zohn et al., 2003). Both NP bending and NT closure involve CE movements, facilitated by changes in the actin cytoskeleton that drive apical constriction and that are regulated by RhoA (Kinoshita et al., 2008; Nishimura et al., 2012; Ybot-Gonzalez and Copp, 1999; Ybot-Gonzalez et al., 2007b).

Whereas actomyosin fulfils a crucial role in neurulation, different actin-dependent mechanisms appear to drive NT closure at distinct levels of the body axis. In fact, cranial closure in embryos is impaired when cytoskeletal dynamics are altered (Brouns et al., 2000; Stumpo et al., 1995; Xu et al., 1998). Indeed, actomyosin contractility within neuroepithelial cells is required for the initiation of NT closure and it is regulated by the Wnt-PCP pathway via RhoA (Ybot-Gonzalez and Copp, 1999; Ybot-Gonzalez et al., 2007b), and Wnt-PCP homozygous and heterozygous mutant embryos have been shown to develop spina bifida (McGreevy et al., 2015; Paudyal et al., 2010; Andersson et al., 2010; Pinson et al., 2000; Suriben

[1]Grupo de Neurodesarrollo, Hospital Universitario Virgen del Rocio/Instituto de Biomedicina de Sevilla (IBIS)/CSIC/Universidad de Sevilla, Sevilla 41013, Spain. [2]Department of Bioengineering, University of Pittsburgh, Pittsburgh, PA 15260, USA. [3]College of Optometry, the Ohio State University, Columbus OH 43210, USA. [4]Centro Andaluz de Biología del Desarrollo (CABD), and CIBERER, Instituto de Salud Carlos III, Universidad Pablo de Olavide-CSIC, Sevilla 41013, Spain. [5]Newlife Birth Defects Research Centre, Institute of Child Health, University College London, 30 Guilford Street, London WC1N 1EH, UK. [6]Unidad de Gestión Clínica de Neurocirugía, Hospital Universitario Virgen del Rocío, Instituto de Biomedicina de Sevilla (IBIS)/CSIC/Universidad de Sevilla, Sevilla 41013, Spain. [7]Unidad de Gestión Clínica de Neurología y Neurofisiología, Hospital Universitario Virgen Macarena, Sevilla 41009, Spain.
*These authors contributed equally to this work

‡Author for correspondence (pybot-ibis@us.es)

B.L., 0000-0002-4338-1830; J.M.C., 0000-0003-4795-3485; R.C.M., 0000-0002-0700-3488; P.Y., 0000-0001-7836-2659

Received 20 July 2017; Accepted 3 April 2018

Development (2018) 145, dev157487. doi:10.1242/dev.157487

et al., 2009). Although many studies have focused on the mechanisms driving neural fold elevation and fusion of the dorsal part of the neural folds at the posterior neuropore (PNP), it still remains unclear how the last step of neurulation is coordinated in the caudal NP.

Rostro-caudal elongation of the mouse embryo benefits from the contribution of bipotent neuromesodermal progenitors (NMPs), cells derived from the caudal epiblast (Garriock et al., 2015; Henrique et al., 2015; Tzouanacou et al., 2009; Wymeersch et al., 2016). These dual-fated cells are progenitors of the caudal neuroectoderm and somatic mesoderm, indicating that induction and formation of the caudal NP is distinct from that of the anterior NP. Here, we aim to elucidate how the Wnt-PCP pathway controls different stages of specification and differentiation, ultimately coordinating the shaping of the caudal NP, and investigate how interfering with this process affects caudal NT closure.

RESULTS

Different elements of the Wnt-PCP signalling pathway are expressed during spinal neurulation

We first set out to define the temporal and spatial expression of Wnt-PCP genes during the later stages of caudal NT closure. NT closure is completed by embryonic day (E) 10 and genes of the Wnt-PCP pathway were specifically detected in the most caudal part of the E9.5 embryo, including the PNP (e.g. *Wnt5a*, *Wnt3a*, *Vangl2*, *Prickle1*, *Gpc4* and *Ptk7*; Fig. 1A-E,K,L). Other Wnt-PCP genes, like *RhoA*, *Daam1* and *Shroom3*, were also expressed in the PNP, but in a more widespread pattern (Fig. 1M-O). Cross-sections of the

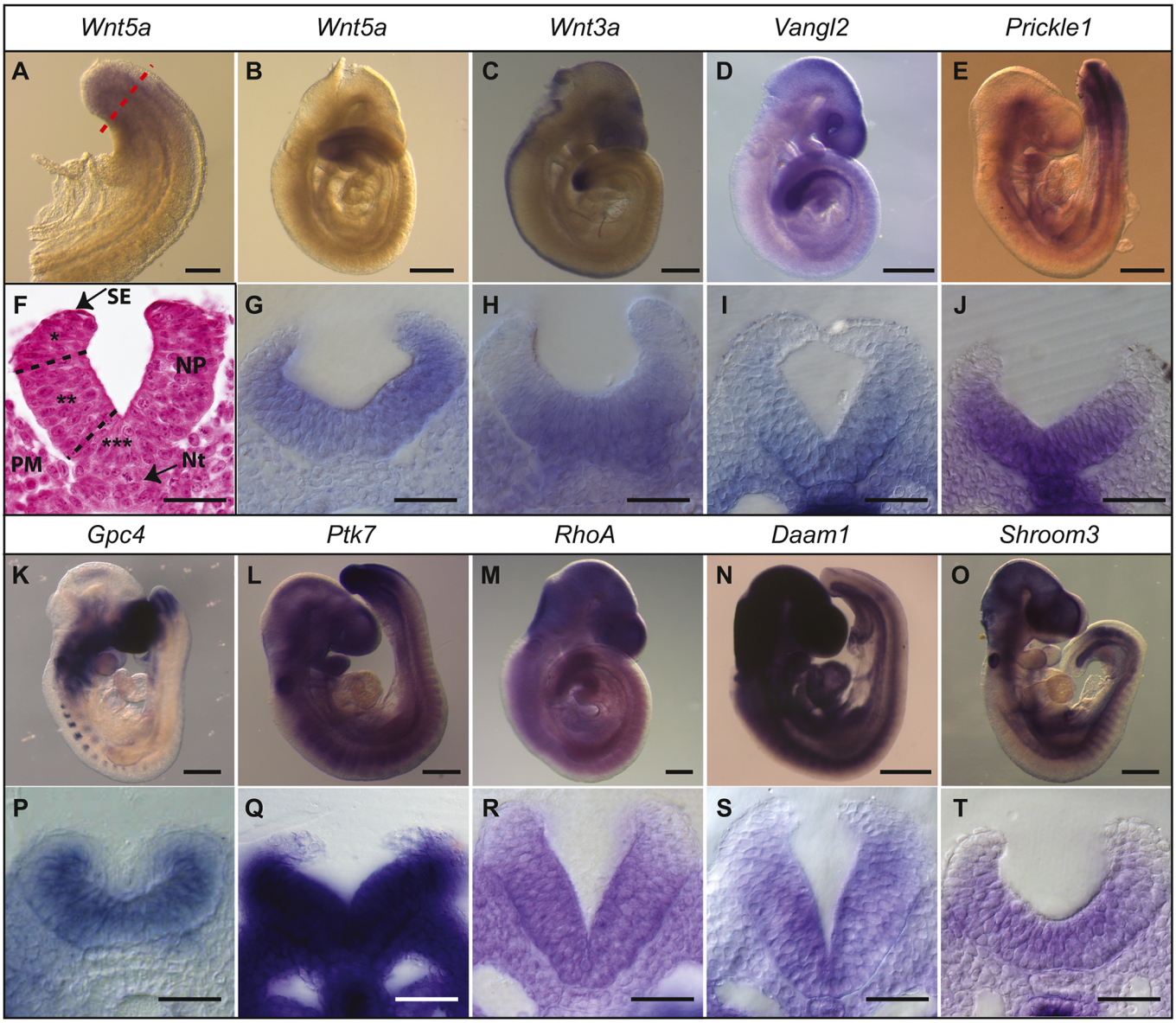

Fig. 1. Elements of the Wnt-PCP pathway expressed at the posterior neuropore. *In situ* hybridisation for *Wnt5a* (A,B,G), *Wnt3a* (C,H), *Vangl2* (D,I), *Prickle1* (E,J), *Gpc4* (K,P), *Ptk7* (L,Q), RhoA (M,R), *Daam1* (N,S) and *Shroom3* (O,T) in E9.5 mouse embryos (B-E,K-O) and corresponding transverse sections through the PNP at the level of the dashed line in A (F-J,P-T). In F, the main tissues and the domains of the neural fold are indicated: PM, paraxial mesoderm; NP, neural plate; Nt, notochord; SE, surface ectoderm. Single asterisk indicates DLHPs; double asterisk indicates the non-bending lateral neural plate; triple asterisk indicates the MHP. Scale bars: 200 µm (A); 500 µm (B-E,K-O); 50 µm (F-J,P-T).

Development (2018) 145, dev157487. doi:10.1242/dev.157487

PNP revealed a broad distribution of these mRNAs across the NP, including the MHP, albeit weaker in the most dorsal part of the neural folds (Fig. 1F-J,P-T). These data indicate that Wnt signalling may be active in the PNP.

Alterations to the Wnt-PCP pathway affect actin distribution and the morphology of the PNP

Homozygous Wnt-PCP mutant embryos develop craniorachischisis, making it difficult to study the role of Wnt-PCP genes during the later stages of NT closure. Thus, heterozygous embryos are a better tool for studying caudal NT defects (NTDs). Analysis of the PNP in *Vangl2*$^{+/+}$ and *Vangl2*$^{+/Lp}$ embryos revealed similar *RhoA* expression and stronger *Prickle1* expression in *Vangl2*$^{+/Lp}$ embryos along with weaker *Daam1* expression (Fig. S1A-C). Quantitative RT-PCR analysis was used to verify these results and to compare stage-matched embryos and although the expression of the genes in the Wnt-PCP pathway appeared to differ in *Vangl2*$^{+/+}$ and *Vangl2*$^{+/Lp}$ embryos, the fold change was not considered significantly different (Fig. S1D). These results suggest that the molecular basis of Wnt-PCP activation might involve other modifications, such as phosphorylation, as previously shown for members of this pathway (Maekawa et al., 1999; Shafer et al., 2011; Yang et al., 2017).

Transverse PNP sections from a *Vangl2*$^{+/Lp}$ embryo revealed morphological effects at E9.5 (Fig. 2A,D), as also observed at earlier stages (Fig. S2A,B). There was a significant outward flexure in the NP of these embryos, with the basal side juxtaposed to the paraxial mesoderm; this region of the neural fold should be straight, as seen in *Vangl2*$^{+/+}$ embryos (Fig. 2D,E, arrowheads; compare with Fig. 2A,B, Fig. S2B,E). This outward flexure is combined with a dorso-ventral reduction in the apico-basal width of the NP (Fig. S3A-C). Morphometric analysis of this region demonstrated that although the dorsal width is similar (46.5 µm in *Vangl2*$^{+/+}$ and 47.2 µm in *Vangl2*$^{+/Lp}$; Fig. S3A,B), the ventral width in *Vangl2*$^{+/Lp}$ embryos (37 µm) was significantly narrower than in *Vangl2*$^{+/+}$ embryos (40 µm; Fig. S3B). Concomitantly, there was a 1.4-fold significant increase in the length of the neural fold in *Vangl2*$^{+/Lp}$ embryos (145.1 µm) relative to *Vangl2*$^{+/+}$ embryos (103.1 µm; Fig. S3C), producing a significant difference in the length/ventral width ratio between *Vangl2*$^{+/Lp}$ and *Vangl2*$^{+/+}$ embryos (Fig. S3D; for more data regarding the sample sizes and statistical analyses in all experiments, see Materials and Methods section and Table S7).

Such outward flexure of the neural folds and the decrease in neural fold width have been observed previously in embryos with altered actin dynamics (Grego-Bessa et al., 2015; Ybot-Gonzalez and Copp, 1999); we therefore assessed the actin microfilament distribution in the NT of *Vangl2*$^{+/Lp}$ embryos. As expected, actin microfilaments are distributed neatly along the apical side of the neural folds in *Vangl2*$^{+/+}$ embryos (Fig. 2B,C), whereas the actin belt was disrupted over the entire lumen of the *Vangl2*$^{+/Lp}$ PNP (Fig. 2E,F, Fig. S2D,E) and this disruption was substantially worse in *Vangl2*$^{Lp/Lp}$ embryos (Fig. S2C,F). In *Vangl2*$^{+/+}$ embryos exposed to cytochalasin D (CytD), a potent inhibitor of actin polymerisation, the apical localisation of F-actin was disturbed and was associated with atypical bending of the lateral NP (Fig. 2G-I) similar to that observed in the neural folds of *Vangl2*$^{+/Lp}$ embryos. Thus, actin microfilaments are required to establish correct PNP morphology.

Activation of Wnt-PCP signalling induces the formation of the Dishevelled-Daam1-RhoA complex, and activates its downstream effector ROCK, leading to cytoskeletal remodelling (Habas et al., 2001, 2003). To analyse the role of actin microfilaments as specific downstream elements in the Wnt-PCP pathway, we blocked ROCK activity with Y-27632. The PNP in *Vangl2*$^{+/+}$ embryos treated with Y-27632 adopted a similar morphology to that in *Vangl2*$^{+/Lp}$ embryos, as described previously (Escuin et al., 2015), with an actin distribution similar to that observed in the NT of embryos treated with CytD (compare Fig. 2J-L with 2D-F and 2G-I). The neural folds of embryos treated with CytD and Y-27632, as in *Vangl2*$^{Lp/+}$ embryos, underwent significant ectopic bending relative to *Vangl2*$^{+/+}$ embryos (P<0.05; Fig. S4).

The Wnt-PCP pathway drives the polarised subcellular accumulation of the contractile actomyosin network during cranial NT closure (Mahaffey et al., 2013; McGreevy et al., 2015; Nishimura et al., 2012; Ossipova et al., 2015). To reveal the distribution of actin in the apical plane of the caudal closing NP, the distribution of phalloidin was analysed in the PNP of flat-mount *Vangl2*$^{+/+}$ embryos (Fig. 2M). There was significantly weaker phalloidin staining in the *Vangl2*$^{+/Lp}$ embryo compared with its wild-type counterpart (Fig. 2N, Fig. S5). In the PNP, actin was organised into two different planar cell arrangements: linear alignment of neighbouring cells with F-actin condensed on one side of the cellular arrangement, forming actin cables (Fig. 2Oi); or accumulation of actin at one vertex of individual cells (Fig. 2Oi,P, Ti). In contrast to the cranial neural ectoderm, the actin cables in the PNP were all oriented in an anteroposterior direction, and they were restricted to the anterior PNP, mainly on the lateral side and corresponding to the neural fold juxtaposed to the paraxial mesoderm (88.5% lateral vs 11.5% central; Fig. 2M,Oi,Q,R). However, significantly fewer linear cell arrangements were evident in *Vangl2*$^{+/Lp}$ PNPs, with variable orientation compared with their wild-type counterparts (Fig. 2N,Oii,Q-S). In addition, we observed a similar basal intensity of actin on the apical side of the boundary between cells but a significant loss of intensity in the polarised actin cumuli in *Vangl2*$^{+/Lp}$ embryos relative to *Vangl2*$^{+/+}$ embryos (Fig. 2Tii,U,V). Unlike the actin cables, these cumuli were distributed throughout the PNP.

Thus, Vangl2 appears to be required for the apical and planar polarised distribution of actin microfilaments in the anterior part of the PNP where the neural folds elevate, and when this distribution is altered, morphological anomalies arise.

Altered PNP morphology as a consequence of mutations in the Wnt-PCP pathway leads to spina bifida

We next explored how the loss of *Vangl2* activity affects caudal neurulation. Analysis of *Vangl2*$^{+/+}$ and *Vangl2*$^{+/Lp}$ embryos (summarised in Table S1) highlighted a tendency towards delayed NT closure in *Vangl2*$^{+/Lp}$ embryos in association with the altered morphology of the intermediate neural folds, although NT closure was not impeded (see Copp et al., 1994).

As craniorachischisis develops in *Vangl2*$^{Lp/Lp}$ homozygous mutants, more severe knockdown of Wnt-PCP signalling was studied at later stages of NT closure in double *Vangl2*$^{+/Lp}$/*Daam1*$^{+/gt}$ mutants. Daam1 belongs to the formin family of actin nucleators, and interacts with Dishevelled and RhoA in the Wnt-PCP pathway (Habas et al., 2001; Sato et al., 2006). No obvious phenotypic differences were observed in the NT of embryos from the three genotypes of the *Daam1* gene trap mouse line at E10.5-E14.5 (*Vangl2*$^{+/+}$/*Daam1*$^{+/+}$, n=45; *Vangl2*$^{+/+}$/*Daam1*$^{+/gt}$, n=79; *Vangl2*$^{+/+}$/*Daam1*$^{gt/gt}$, n=20; Fig. 3A,C; data not shown). However, there was a higher incidence of spina bifida in the *Vangl2*$^{+/Lp}$/*Daam1*$^{+/gt}$ line (6/27, 22.22%; Fig. 3B,E) relative to *Vangl2*$^{+/Lp}$/*Daam1*$^{+/+}$ mice (1/16, 6.25%; Fig. 3D). Histological analysis revealed exacerbated angles of the neural folds at the

Development (2018) 145, dev157487. doi:10.1242/dev.157487

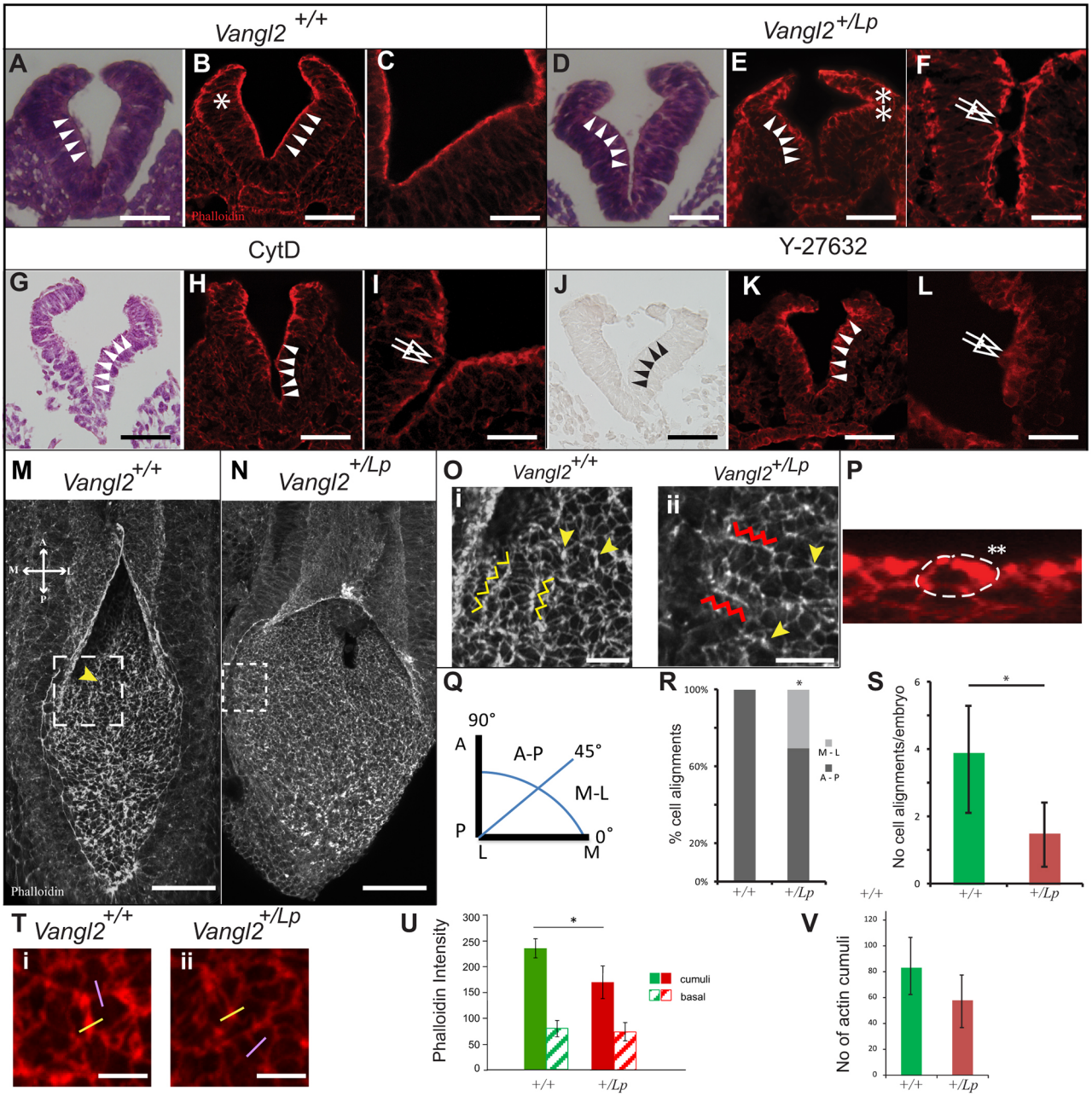

Fig. 2. Disrupted neural fold morphology and apical actin distribution in E9.5 *Vangl2*$^{+/Lp}$ embryos, and in embryos treated with cytochalasin D and Y-27632. (A-L) Transverse sections through the PNP (see plane of the section in Fig. 1A) of *Vangl2*$^{+/+}$ (A-C), *Vangl2*$^{+/Lp}$ (D-F), cytochalasin D-treated *Vangl2*$^{+/+}$ (G-I) and Y-27632-treated *Vangl2*$^{+/+}$ (J-L) embryos. (A,D,G,J) H&E staining; (B,C,E,F,H,I,K,L) phalloidin labelling. Arrowheads in A and B indicate the straight wild-type neural fold; note, by contrast, the outward flexion induced by mutation or treatment (D,E,G,H,J,K). Asterisk in B marks the curved DLHP of *Vangl2*$^{+/+}$ embryo; double asterisk in E marks the angle of the DLHP in the *Vangl2*$^{+/Lp}$ embryos. White arrows in F,I,L point to disruption of the apical actin belt. (M,N) Dorsal views of phalloidin-stained flat-mount PNPs from *Vangl2*$^{+/+}$ and *Vangl2*$^{+/Lp}$ embryos, respectively. (Oi-Oii) Magnification of the boxed areas in M and N, respectively. Yellow/red carets indicate cables of F-actin condensation on one side of aligned cells (mediolateral in Oi; anteroposterior in Oii); yellow arrowheads indicate cumuli of F-actin at one vertex of individual cells. (P) Orthogonal view of the cell marked in M by the yellow arrowhead, and outlined here, with a double asterisk marking the area of polarised actin cumuli. (Q) Diagram of cell alignment relative to the mediolateral axis of the embryo (0-45°, mediolateral orientation; 45-90°, anteroposterior orientation). (R) Proportion of cell alignments in anteroposterior (A-P; dark grey) or mediolateral (M-L; light grey) orientation (A-P orientation: 100% in *Vangl2*$^{+/+}$ vs 69.23% in *Vangl2*$^{+/Lp}$ embryos: **P*<0.05). (S) Number of cell alignments in *Vangl2*$^{+/+}$ (3.71 lines/embryo) and *Vangl2*$^{+/Lp}$ (1.4/embryo) embryos. (Ti,Tii) Magnification of an area of phalloidin-stained PNT showing an actin cumulus in *Vangl2*$^{+/+}$ (Ti) and *Vangl2*$^{+/Lp}$ (Tii) embryos. (U) Phalloidin intensity of the plot profile obtained from selected ROIs crossing the actin cumuli (solid bar) and basal actin at the linear boundary of two neighbouring cells (striped bar; yellow lines and purple lines, respectively, in Ti and Tii). (V) Graph of the number of actin cumuli in *Vangl2*$^{+/+}$ and *Vangl2*$^{+/Lp}$ embryos. Error bars represent s.e.m. **P*<0.05. Scale bars: 50 µm (A,B,D,E,G,H,J,K,M,N); 25 µm (C,F,I,L); 12.5 µm (Oi,Oii); 6.25 µm (Ti,Tii).

dorsolateral hinge points (DLHPs) in *Vangl2*$^{+/Lp}$/*Daam1*$^{+/gt}$ embryos with spina bifida at E10.5, contrasting with the straight lateral sides of the NT associated with the closed PNP in *Vangl2*$^{+/+}$/*Daam1*$^{+/+}$ embryos (Fig. 3F,G). Indeed, the phenotype of the *Vangl2*$^{+/Lp}$/*Daam1*$^{+/gt}$ embryos was reminiscent of the early *Vangl2*$^{+/Lp}$ neural fold malformations (Fig. 2D). The straight region

Development (2018) 145, dev157487. doi:10.1242/dev.157487

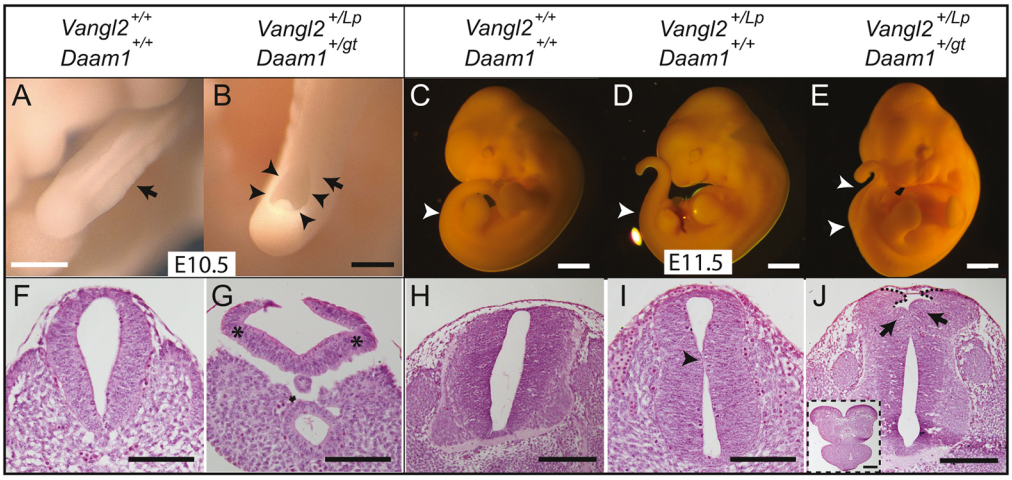

Fig. 3. Downregulation of Wnt-PCP signalling leads to spina bifida. (A-J) E10.5 (A,B) and E11.5 (C-E) embryos of the indicated genotypes and corresponding H&E-stained transverse sections through the caudal region (F-J). Black arrows in A and B indicate the transverse section level shown in F and G, respectively. Arrowheads in B indicate spina bifida. White arrowheads in C-E indicate the level of the transverse sections in H-J, as well as the spina bifida in E. Top arrowhead corresponds to the axial level for the section in the inset in J and bottom arrowhead corresponds to the axial level of the section in J. Asterisks in G mark DLHP of the neural folds, with an exacerbated angle. Black arrowhead in I indicates an outward kink. Black arrows in J indicate aberrant dorsal bending on both sides of the distorted neural tube. Dotted line indicates unfused dorsal tips of neural folds. Inset in J shows a section through the open spina bifida at the level marked by the top arrowhead in E. Scale bars: 50 µm (A,B); 1 mm (E,C,D); 100 µm (F,G,I); 200 µm (H,J,J inset).

of the NT of E11.5 *Vangl2*$^{+/+}$/*Daam1*$^{+/+}$ embryos (Fig. 3H) has a slight outward kink in *Vangl2*$^{+/Lp}$/*Daam1*$^{+/+}$ embryos (Fig. 3I), whereas the sections anterior to the open NT displayed a characteristic malformation of the dorsal part of the lateral NT in *Vangl2*$^{+/Lp}$/*Daam1*$^{+/gt}$ embryos with spina bifida (Fig. 3J). Thus, exacerbated outward flexion of the neural fold may be responsible for the failure in dorsal closing (Fig. 3J, inset).

Our results indicate that disrupted PCP-Wnt signalling affects neural fold morphology, inducing aberrant bending that separates the dorsal tips of the neural folds and impedes correct caudal NT closure, inducing spina bifida.

Disruption of the Wnt-PCP pathway affects apical cell morphology

Cadherins, together with β-catenin in adherens junctions and ZO1 (Tjp1) at tight junctions, regulate cytoskeletal actin assembly, anchoring the actomyosin cytoskeleton to the cell membrane before apical constriction in these cells (Nishimura and Takeichi, 2009). Thus, we assessed whether the apical region of the cell is distorted in the lateral neural fold as a consequence of disrupting Wnt-PCP signalling or actin polymerisation. N-cadherin (Cdh2) can be controlled by Vangl2 (Nagaoka et al., 2014) and its distribution in adherens junctions is disrupted in the neural folds of *Vangl2*$^{+/Lp}$ embryos, as well as in embryos treated with CytD and Y-27632 (Fig. 4A-D). Similar disruption of ZO1 and β-catenin was observed (Fig. S6). To quantify the apical cell arrangement, we used either a tilted section or a 3D image of 50-µm-thick sections of the elevating neural folds immunolabelled for ZO1. The mean apical area of the closing neural fold cells in *Vangl2*$^{+/Lp}$ and *Vangl2*$^{Lp/Lp}$ embryos increased significantly with respect to the *Vangl2*$^{+/+}$ embryos (Fig. 4E-I). Similarly, embryos treated with either CytD or Y-27632 reproduced the phenotype of *Vangl2* mutant embryos (Fig. 4E-M; summarised in Table S2). This expansion in the apical cell surface area due to actin microfilament disorganisation could explain the inappropriate bending of the neural folds in these embryos.

Together, these data indicate that Vangl2 shapes the neural folds by regulating apical actomyosin recruitment and intercellular adhesion.

The Wnt-PCP pathway controls shaping of the PNP by apical cell constriction and cell reorganisation into rosettes

Having established that the apical face of the closing neural folds is affected in *Vangl2*$^{+/Lp}$ and *Vangl2*$^{Lp/Lp}$ embryos, we investigated the origin of the morphological NP malformation. A dorsal view of the PNP revealed *Vangl2* and *Daam1* expression in the lateral and more caudal PNP (Fig. S7A,B), a distribution similar to but more dispersed than that of *RhoA* (Fig. S7C). The caudal NP was very proliferative (Fig. S7D). We studied the apical cell domain in the entire PNP, which includes the node-streak border and the caudal lateral epiblast (hereafter NSB/CLE). NMPs originate in this region (neural cell precursors; Fig. 5E), as well as in the pre-NT (PNT) where the neural folds start to elevate and that mostly houses NMPs (Fig. 5E; Henrique et al., 2015; Wymeersch et al., 2016). ZO1 staining of E9.5 *Vangl2*$^{+/+}$ embryos (n=6) highlighted the apical cell organisation in the PNP (Fig. 5A). Maximum projections of confocal images were segmented to obtain the area of the apical cell domain, the presence of rosettes, and the number of vertices and their order (number of cells that meet at that vertex). The PNT was divided into two zones (see Fig. 5E), a central zone that included the midline and a peripheral zone that takes in the neural folds. Surprisingly, the mean apical cell area did not differ between the two zones (7.35 µm^2 and 7.46 µm^2, respectively), the average in the PNT being 7.43 µm. However, the average cell size in the NSB/CLE was 11.5 µm^2, with a significant increase in the apical domain of the cells from the NSB/CLE compared with the PNT (see Table S3). Hence, apical cell contraction appears to occur in a caudal-rostral direction.

Multicellular rosettes have been correlated with the epithelial cell rearrangements that drive CE in many species (Lienkamp et al., 2012; McGreevy et al., 2015). Cells formed rosettes within the PNP of *Vangl2*$^{+/+}$ embryos; however, their distribution across the PNP was not uniform, and they were more concentrated in the PNT (16.6%) than in the NSB/CLE (8.1%: Table S3). When we analysed the two regions that form the PNT, we observed similar proportions in both zones (17.6% rosettes in the central and 16% in the peripheral zone). Rosette formation is associated with a reduced apical area, a process linked to tissue folding during morphogenesis

Development (2018) 145, dev157487. doi:10.1242/dev.157487

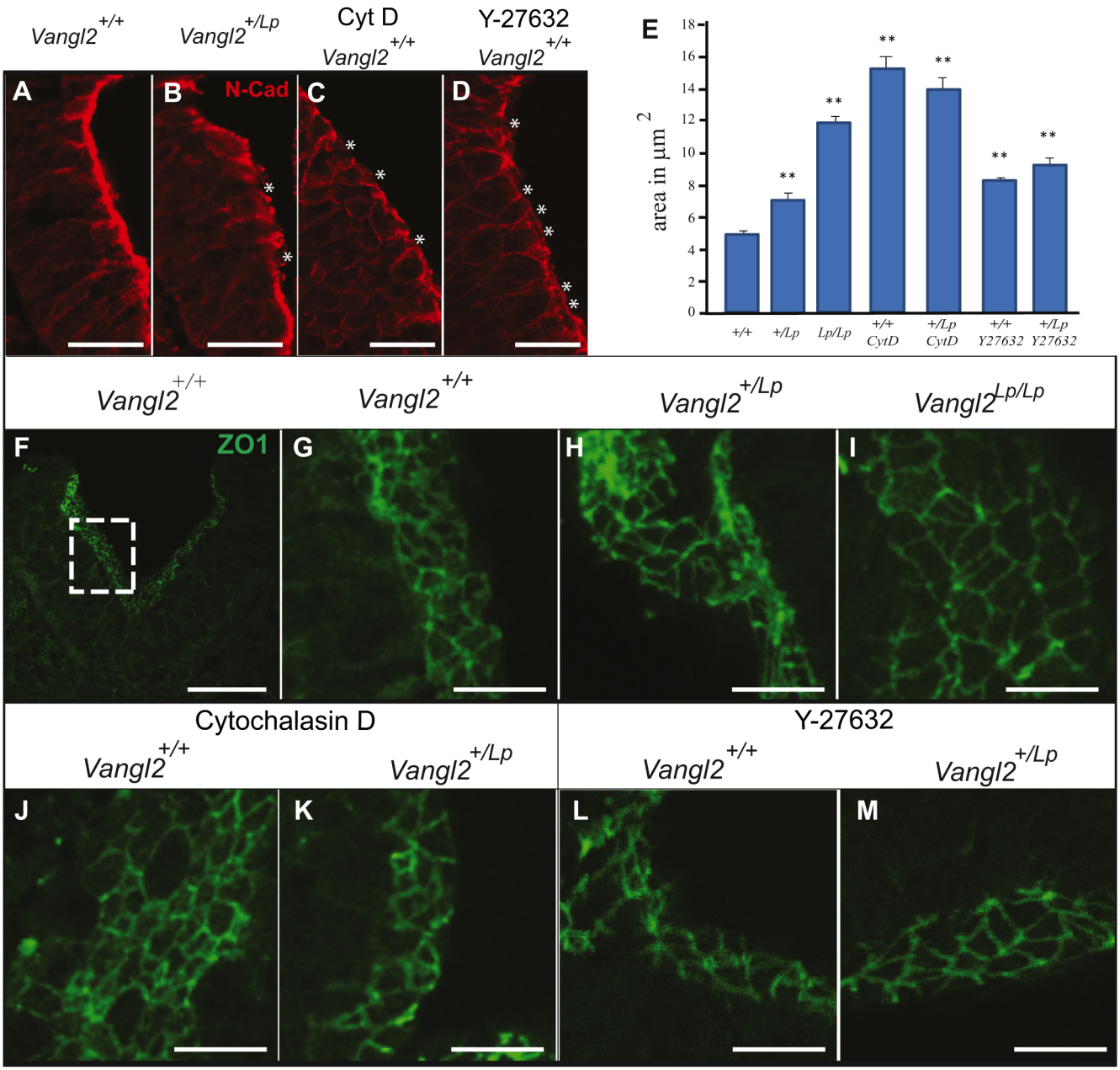

Fig. 4. Planar cell arrangement in the neural folds is disrupted in *Vangl2*$^{+/Lp}$, *Vangl2* $^{Lp/Lp}$, CytD- and Y-27632-treated embryos. (A-D) Transverse neural fold sections from *Vangl2*$^{+/+}$ (A), *Vangl2*$^{+/Lp}$ (B), CytD-treated (C) and Y-27632-treated (D) embryos immunolabelled for N-cadherin. Asterisks in B-D indicate disruption of apical N-cadherin. (E) Average apical cell area (µm^2±s.e.m.) in *Vangl2*$^{+/+}$ (+/+), *Vangl2*$^{+/Lp}$ (+/*Lp*) *Vangl2*$^{Lp/Lp}$ (*Lp*/*Lp*), CytD- and Y-27632-treated embryos. ***P*<0.001 compared with *Vangl2*$^{+/+}$. (F-M) Transverse sections of the PNP of the indicated genotypes, untreated or treated with cytochalasin D or Y-27632, immunolabelled for ZO1. Dashed box in F indicates the apical side of the neural fold and the region where the apical areas were measured in all embryos. Scale bars: 50 µm (A,B,F); 25 µm (C,D); 12.5 µm (G-M).

(Harding et al., 2014). Indeed, there was a reduction in the average apical cell area in the PNT when cells forming rosettes were analysed separately (from 7.65 µm^2 to 6.28 µm^2; Fig. 5B,I, Table S3). Thus, apical constriction of cells in the entire caudal neural ectoderm elicits bending of the PNP in association with cellular rosette formation, which progresses in a caudo-rostral direction.

Interestingly, there was a significant increase in apical cell area in the PNT of *Vangl2*$^{+/Lp}$ embryos (n=4) relative to *Vangl2*$^{+/+}$ embryos (a 1.5-fold increase), which was also evident in the cells that form rosettes (Table S3, Fig. 5I). This 1.5-fold increase in apical cell size was also observed in the NSB/CLE (Table S3). Moreover, the *Vangl2*$^{+/Lp}$ PNT had significantly fewer rosettes than did *Vangl2*$^{+/+}$ embryos, as well as fewer higher order rosettes (rosettes formed by more than five cells in the vertex; Fig. 5C,D,F-H, Table S3). When we analysed the sub-zones of the PNT, although both had significantly fewer rosettes than *Vangl2*$^{+/+}$ embryos, there was a significantly lower proportion of rosettes (6.7%) in the peripheral zone than in the central zone (8.7%; Table S3). This reduction of rosettes in the *Vangl2*$^{+/Lp}$ PNT also affected the NSB/CLE area, where only 3.1% of rosettes were located and no higher order rosettes were observed (Fig. 5H). Thus, the morphological

Development (2018) 145, dev157487. doi:10.1242/dev.157487

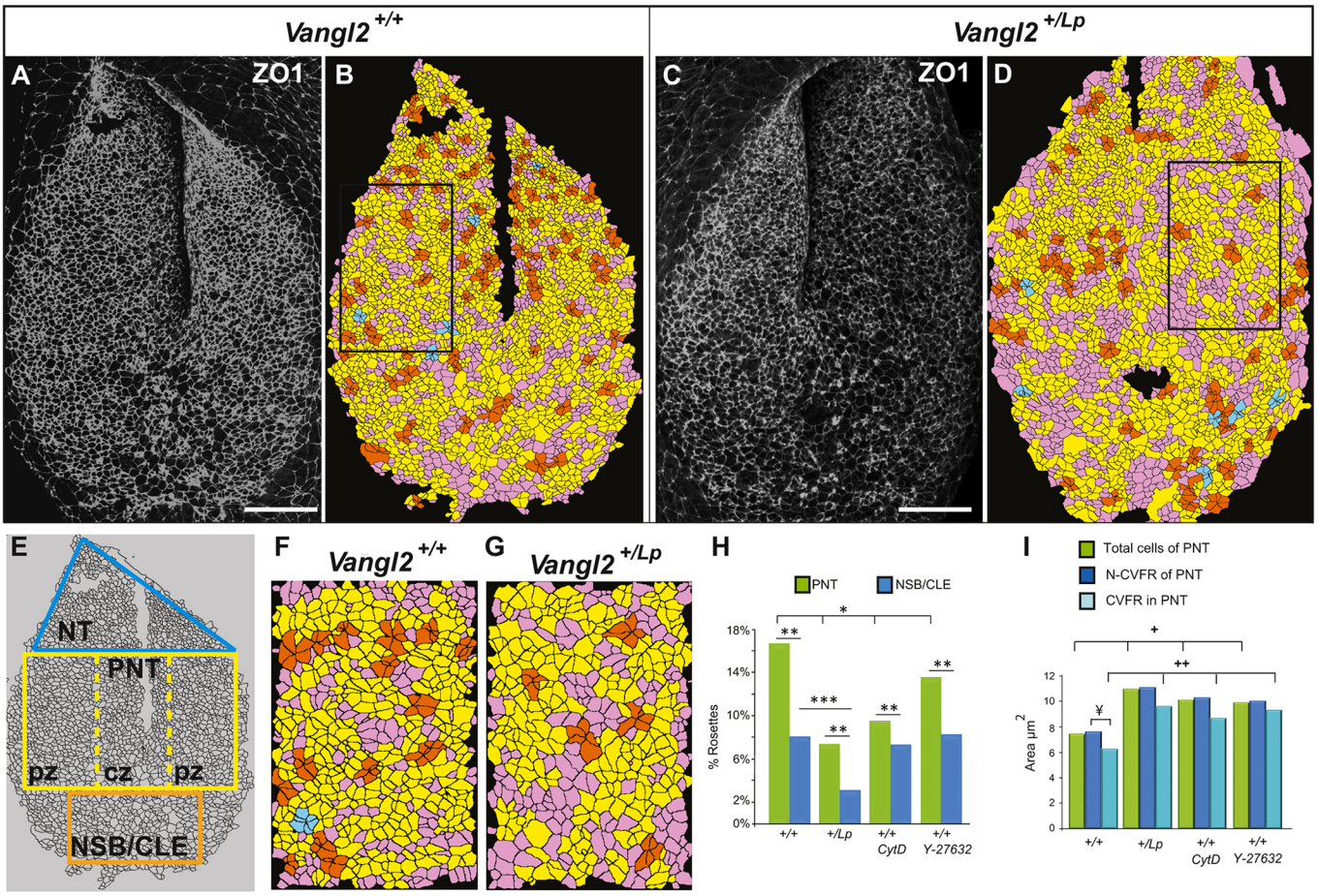

Fig. 5. Altered apical cell constriction and cell reorganisation into rosettes at the PNP of *Vangl2*$^{+/Lp}$, *Vangl2*$^{Lp/Lp}$, CytD- and Y-27632-treated embryos. (A-D) Dorsal views of the PNP of E9.5 *Vangl2*$^{+/+}$ (A,B) and *Vangl2*$^{+/Lp}$ (C,D) embryos. (A,C) ZO1 immunolabelling. (B,D) Confocal images segmented with Seedwater Segmenter, and imported to ImageJ to define the rosettes. Cells were colour-coded based on the number of cells that meet at shared vertices: orange, 5-cell rosette; blue, 6-cell rosette. Cells that shared vertices with 4 or 3 cells are in yellow and pink, respectively (not considered rosettes). (E) Diagram illustrating the regionalisation of the PNP: NT, neural tube; PNT, preneural tube; pz, peripheral zones; cz, central zone; NSB/CLE, the node-streak border and the caudal lateral epiblast. (F,G) Magnifications of the PZ (outlined in B and D, respectively). (H) Percentage of cells in rosettes in the PNT and in the NSB/CLE under the four different conditions. (I) Mean apical cell area (µm^2) in the PNT, differentiating between: total cell population; cells not forming rosettes (N-CVFR); cells with a vertex forming rosettes (CVFR) in the four different conditions. Symbols all indicate significant differences (P<0.05) between specific cell populations as indicated by the brackets. Scale bars: 50 µm.

changes in *Vangl2*$^{+/Lp}$ embryos resulting from altered apical constriction generates 1.5-fold larger apical areas in the entire PNP and fewer multicellular rosettes, leading to a 1.4-fold increase in the length of the neural fold (Fig. S3D).

CytD (n=4; Fig. S8A,B) and Y-27632 (n=4; Fig. S8C,D) also increased the apical cell area in the PNT, and the number of cells forming rosettes (Fig. 5I, Table S3), indicating that the alterations in *Vangl2*$^{+/Lp}$ embryos were provoked by actin microfilament disorganisation. CytD and Y-27632 also significantly reduced the total number of rosettes per PNT and NSB/CLE relative to *Vangl2*$^{+/+}$ embryos (Fig. 5H, Table S3).

The molecular motor non-muscle myosin-IIB heavy chain (MHC-IIB), together with F-actin, is involved in apical constriction. Immunolabelling revealed a scattered distribution of MHC-IIB in the *Vangl2*$^{+/+}$ PNP, with more concentrated expression in the NSB/CLE area (Fig. 6A, Fig. S9A), a distribution distinct to that in the cranial NT (McGreevy et al., 2015). The *Vangl2*$^{+/Lp}$ PNP exhibited a more abundant and intricate MHC-IIB meshwork, although some individual cells were also observed (Fig. 6D, Fig. S9B). Vangl2 lies downstream of Wnt-PCP and it regulates Rho kinases, which phosphorylate myosin light chain, the key regulator of non-muscle myosin-IIB (Ybot-Gonzalez et al., 2007b; Etienne-Manneville and Hall, 2002). In *Vangl2*$^{+/+}$ embryos, phosphorylated myosin-IIB (p-MLC) was found to be condensed either medioapically or in pairs of cumuli in neighbouring cells forming dense supracellular p-MLC-actin structures (Fig. 6G-I″). Interestingly, a similar apical localisation of p-MLC has been described for apical contractile pulses during *Drosophila* gastrulation (Martin et al., 2009; Mason et al., 2013; Vasquez et al., 2014). By contrast, *Vang2*$^{+/Lp}$ cells in the PNP accumulated p-MLC across the entire apical domain, in both the junctional and apical domain and they failed to concentrate medioapically. Although similar numbers of p-MLC pairs formed in *Vang2*$^{+/Lp}$ as in *Vangl2*$^{+/+}$ embryos, there was an abnormal distance between them (*Vang2*$^{+/Lp}$ 1.85 µm vs *Vangl2*$^{+/+}$ at 1.34 µm; P<0.05; Fig. 6J-M).

Hence, the continuous shaping of the PNP appears to be initiated in the most caudal part of the wild-type PNP, mainly involving actomyosin apical cell constriction, probably caused by pulse contraction. Towards more anterior regions of the PNP, and in

Development (2018) 145, dev157487. doi:10.1242/dev.157487

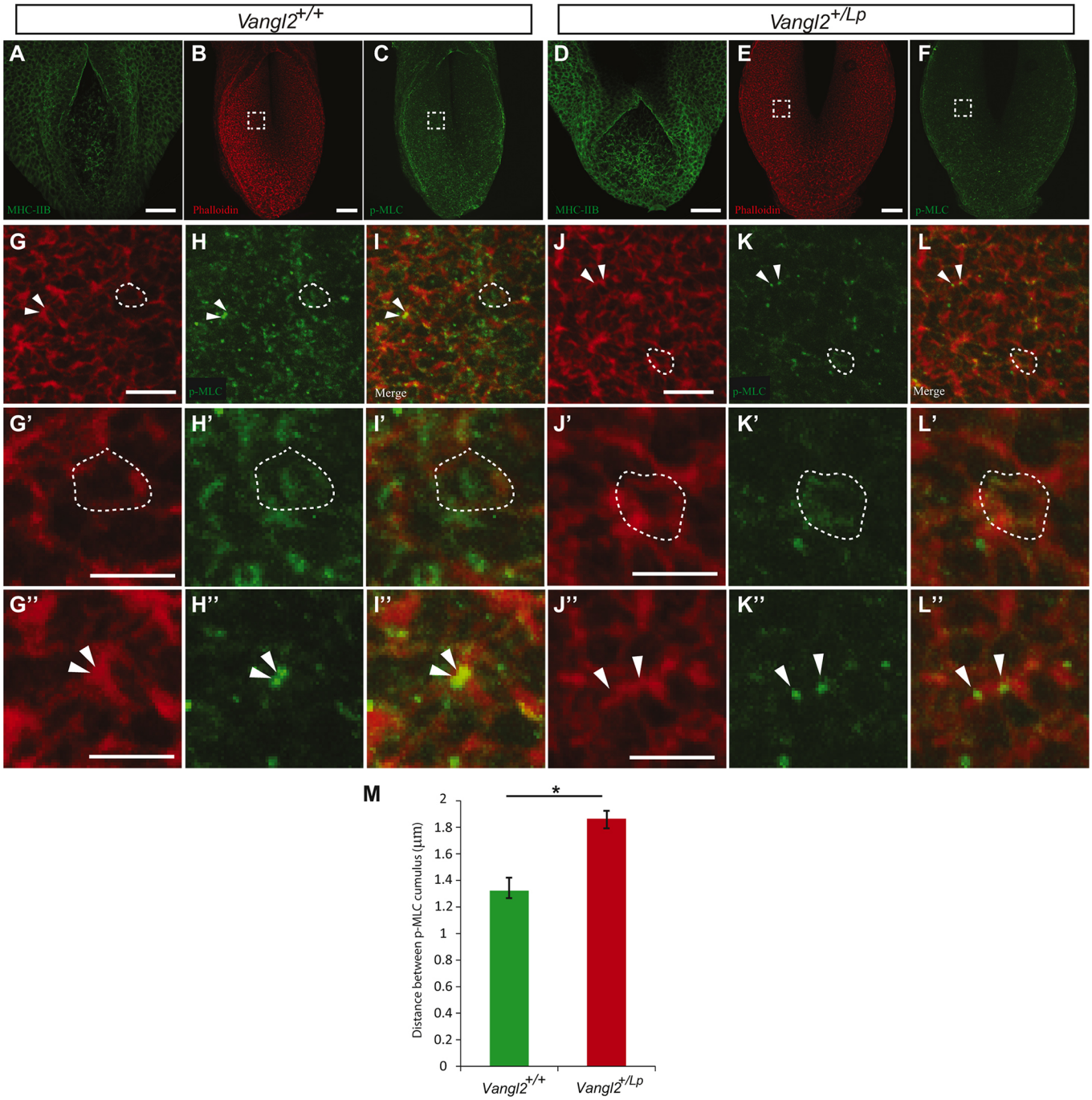

Fig. 6. Mutation of the *Vangl2* gene disrupts the supracellular actomyosin meshwork. (A-L″) Dorsal view of PNP from *Vangl2*$^{+/+}$ (A-C) and *Vangl2*$^{+/Lp}$ (D-F) embryos labelled with anti-MHC-IIB (A,D), phalloidin (B,E) or anti-p-MLC (C,F). G, H, J and K are magnifications of the insets in B, C, E and F, respectively; I and L are merged panels of G,H and J,K, respectively; H′-I′ are medioapical condensations of p-MLC in a cell outlined in G-I; K′-L′ show the failed medioapical condensation of p-MLC evident at the junction and dispersed p-MLC indicated by the dashed outline in J-L. G″-I″ (*Vangl2*$^{+/+}$) and J″-L″ (*Vangl2*$^{+/Lp}$) show paired cumuli of p-MLC, as marked by the arrowheads in G-L. (M) Difference between the distance of paired p-MLC cumuli in the *Vangl2*$^{+/+}$ and *Vangl2*$^{+/Lp}$ PNT. *P<0.05. Error bars indicate s.e.m. Scale bars: 50 µm (A-F); 12.5 µm (G-L); 6.25 µm (G′-L″).

conjunction with the differentiation process, more complex mechanisms of tissue folding are acquired, all regulated by the Wnt-PCP pathway.

NMP fate in the PNP is not determined by the *Vangl2* genotype

In addition to the average increase in the apical cell area, we found a population of cells in the PNT of *Vangl2*$^{+/Lp}$ embryos that were generally bigger than the larger cells in *Vangl2*$^{+/+}$ embryos; these large cells are referred to hereafter as 'giant cells' (≥13 µm^2; Fig. 7A). The giant cells in *Vangl2*$^{+/+}$ embryos are mainly located in the NSB/CLE where 40% of the population were giant cells, compared with 21% in the PNT. We investigated whether this reduction follows a caudo-rostral progression by analysing the most anterior region of the PNP, the NT (Fig. 5E), in which giant cells represent only 15.6% of the population. Giant cells were more

Development (2018) 145, dev157487. doi:10.1242/dev.157487

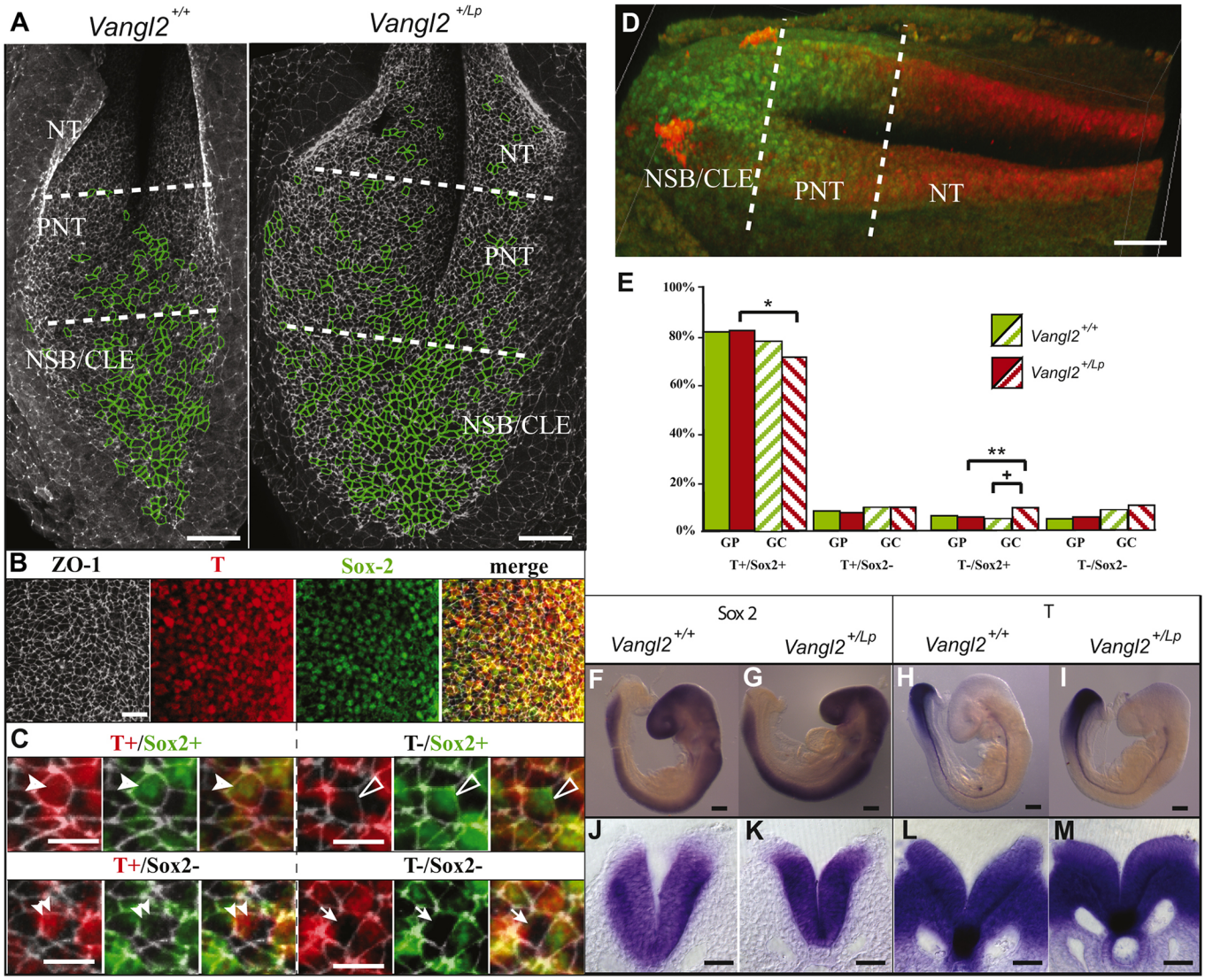

Fig. 7. The progressive differentiation of neuromesodermal progenitors in the PNP is not affected by *Vangl2* heterozygosity. (A) Dorsal view of the PNP of E9.5 *Vangl2*$^{+/+}$ and *Vangl2*$^{+/Lp}$ embryos immunolabelled for ZO1 (grey), with giant cells (≥13 µm^2) outlined in green. (B) Immunolabelling for ZO1 (grey), T (red), Sox2 (green) and the merged image in a section of the PNT showing the four cell types. (C) Magnification of NMPs (T$^+$/Sox2$^+$, arrowheads), neural cells (T$^-$/Sox2$^+$, open arrowheads), mesodermal cells (T$^+$/Sox2$^-$, double arrowheads) and unidentified cells (T$^-$/Sox2$^-$, arrows). In each set of images, left-hand panel shows ZO1/T immunolabelling, middle panel ZO1/Sox2 immunolabelling and right-hand panel ZO1/T/Sox2 merged images. (D) 3D image of the PNP labelled with Sox2 (red) and T (green). (E) Graph of the different cell types in the PNT of *Vangl2*$^{+/+}$ (green) and *Vangl2*$^{+/Lp}$ (red) embryos in both the general population (GP, solid bars) and in the subpopulation of giant cells (GC striped bars). **P*<0.05, significant difference between the percentage of T$^+$/Sox2$^+$ cells in the GC population compared with the general population of the PNT in *Vangl2*$^{+/Lp}$ embryos; ***P*<0.05, significant difference between the percentage of T$^-$/Sox2$^+$ cells in the GC population compared with the general population of the PNT in *Vangl2*$^{+/Lp}$ embryos; $^+$*P*<0.05, significant difference between the percentage of T$^-$/Sox2$^+$ cells in the GC population of the *Vangl2*$^{+/+}$ and *Vangl2*$^{+/Lp}$ embryos. (F-I) *In situ* hybridisation of *Sox2* (F,G) and *T* (H,I) expression in *Vangl2*$^{+/+}$ (F,H) and *Vangl2*$^{+/Lp}$ embryos (G,I), and the corresponding transverse sections through the PNP (J-M). The divisions of the PNP (NT, PNT and NSB/CLE) are defined in A and D. Scale bars: 25 µm (A); 12.5 µm (B); 6.25 µm (C); 50 µm (D,J-M); 200 µm (F-I).

abundant and widespread in *Vangl2*$^{+/Lp}$ than in *Vangl2*$^{+/+}$ embryos, representing 57% of the total population in the NSB/CLE, 42% in the PNT and a 31.3% in the NT (Fig. 7A). Thus, there was a caudal-rostral reduction in the proportion of giant cells in *Vangl2*$^{+/+}$ and *Vangl2*$^{+/Lp}$ embryos.

The distribution of giant cells in the PNP resembles that of MHC-II (Fig. S9A). In fact, whereas 30.8% of the giant cells in the *Vangl2*$^{+/+}$ PNP were MHC-II positive, this figure increased significantly to 75.7% in the PNP of *Vangl2*$^{+/Lp}$ embryos. In the small cell population (apical area <13 µm^2) the apical accumulation of MHC-II did not vary between these two genotypes (20.3% in *Vangl2*$^{+/+}$ and 22.97% in *Vangl2*$^{+/Lp}$; Fig. S9A-D).

The rostral and lateral part of the CLE houses NMPs (Wymeersch et al., 2016), which initially express both T (mesoderm marker) and Sox2 (neural marker) (Tsakiridis et al., 2014). The downregulation of Wnt promotes neural differentiation (van de Ven et al., 2011) and, thus, we analysed the nature of the giant cells to determine whether the *Vangl2* mutation also affected the development and differentiation of NMPs in the PNP. *z*-stacks of confocal images demonstrated that NMPs (T$^+$/Sox2$^+$) constituted 82% of the PNT in *Vangl2*$^{+/+}$ embryos, whereas 8% of the cells had already differentiated towards a mesodermal fate (T$^+$/Sox2$^-$) and 5.6% to a neuronal fate (T$^-$/Sox2$^+$) (4.4% of the cells were of unknown nature as they were T$^-$/Sox2$^-$; Fig. 7B-D; Movie 1). Similar

Development (2018) 145, dev157487. doi:10.1242/dev.157487

proportions were detected in the homologous region of *Vangl2*$^{+/Lp}$ embryos (82.1% T^{+}/Sox2^{+}; 7.3% T^{+}/Sox2^{-}; 5.2% T^{-}/Sox2^{+}; 5.4% T^{-}/Sox2^{-}) indicating that NMP fate in the PNT was not affected by the *Vangl2* genotype (Fig. 7E, Table S4).

NMPs had a significantly larger apical cell area than cells that differentiated further in *Vangl2*$^{+/+}$ and *Vangl2*$^{+/Lp}$ embryos (Table S4). However, all cell types in the *Vangl2*$^{+/Lp}$ embryos had a larger apical area than their counterparts in the *Vangl2*$^{+/+}$ embryos. The PNT contained more giant neural cells (T^{-}/Sox2^{+}) in *Vangl2*$^{+/Lp}$ than *Vangl2*$^{+/+}$ embryos (Fig. 7E, Table S4). Indeed, NMPs were under-represented within the PNT of the *Vangl2*$^{+/Lp}$ embryos, whereas neural cells were over-represented among the giant cells relative to the general population (Fig. 7E, Table S4). Finally, the extent and intensity of *T* and *Sox2* mRNA expression was not altered in the *Vangl2*$^{+/Lp}$ embryos relative to their *Vangl2*$^{+/+}$ littermates (Fig. 7F-M). In summary, the differentiation of NMPs does not appear to be altered in the PNP of *Vangl2*$^{+/Lp}$ embryos, although the increased apical cell size of PNP cells in *Vangl2*$^{+/Lp}$ embryos apparently has a stronger impact on neural cells.

DISCUSSION

The role of the Wnt-PCP pathway during neurulation has become clearer in recent years. Mice carrying mutations in certain Wnt-PCP genes develop craniorachischisis, demonstrating the importance of this pathway in the formation of the NP midline and in the initiation of NT closure, fuelling interest as to how the Wnt-PCP pathway influences these events. Here, we describe the cell behaviour underlying the folding of the caudal neural ectoderm and we identify distinct apical mechanisms that are acquired gradually, showing that Wnt-PCP is required to coordinate such cellular reorganisation. We also demonstrate the caudo-rostral dynamics of progression towards cell differentiation (Henrique et al., 2015). These observations define sequential epithelial tissue dynamics unique to the caudal NP, and the role of Wnt-PCP signalling in the closure and differentiation of the spinal NT.

All cell types participate in the dynamic apical mechanisms that shape the PNP

Two morphological processes are active during NT closure in mice: inflection of the cranial neural tissue where the neural folds begin and where they are well separated; and zipping from the point of closure to close the neuropore (Galea et al., 2017; Massarwa and Niswander, 2013). However, zipping is an anteroposterior process that fuses the dorsal neural folds, whereas for the PNP to achieve an appropriate shape it must first undergo posterior-to-anterior folding. Here, we show that the apical plane of the caudal NP has a continuous network of tight and adherens junctions at the apical cell borders (marked by ZO1, F-actin and N-cadherin), unifying the precursors and more differentiated cells in the PNP, and allowing the tissue to fold into a tube. In addition, we describe a progressive acquisition of more complex mechanisms of apical constriction in conjunction with caudo-rostral dynamics of cell differentiation (Henrique et al., 2015).

In the caudal part of the PNP we found that actomyosin contraction seems to be the main mechanism responsible for folding, which is maintained to a lesser extent in the anterior regions of the PNP. The presence of paired p-MLC cumuli in adjacent cells, colocalising with actin cumuli, suggests the existence of supracellular p-MLC-actin foci. The stability of these foci is perturbed in the *Vangl2*$^{+/Lp}$ PNP, probably owing to the loss of intercellular cytoskeletal and cell adhesion integrity. These supracellular p-MLC-actin foci appear to be analogous to the punctuated actin contractions regulated by the Wnt-PCP pathway during *Xenopus* gastrulation (Kim and Davidson, 2011). Moreover, the distribution of MHC-IIB and the medioapical condensation of p-MLC in the PNP resemble the myosin assembly and disassembly cycles associated with apical pulses of constriction during *Drosophila* gastrulation (Martin et al., 2009; Mason et al., 2013; Vasquez et al., 2014). These cycles of myosin are affected in *Drosophila* mutants with modified myosin phosphorylation. These mutants display more continuous apical myosin-IIB assembly that alters the apical F-actin distribution and decreases the rate of apical constriction (Vasquez et al., 2014). Thus, we propose that myosin-IIB assembles apically and forms crosslinks with the apical F-actin network to induce apical contraction, which is followed by its disassembly. The disorganisation of F-actin evident in *Vangl2*$^{+/Lp}$ embryos would produce a more continuous apical distribution of myosin-IIB that is unable to bind to the F-actin network or to coalesce medioapically, and that fails to bring together supracellular p-MLC-actin cumuli. This disorganisation will reduce the rate of apical contraction, as seen in the giant cells of the *Vangl2*$^{+/Lp}$ embryos. PNP cells may undergo pulsatile rather than continuous contraction to accommodate the cytoskeletal organisation of a tissue undergoing differentiation. Such contractions would remodel the actomyosin networks in pulses, not only to shape the tissue but also altering the cellular patterning of the tissue, generating a morphogenetic neuroepithelium as suggested previously (Vasquez et al., 2014). These events deserve further study to characterise the underlying cell behaviours.

There is a gradual caudo-rostral formation of Wnt-PCP-dependent cellular rosettes, with fewer rosettes forming when this pathway is disrupted (Trichas et al., 2012). Indeed, we found that *Vangl2*$^{+/Lp}$ embryos generate fewer and less complex epithelial rosettes, with the peripheral zone the most affected region of the PNT. Cadherins, linked to and dependent on a well-structured F-actin network, are key elements in the cell intercalation that occurs during epithelial rosette formation (Blankenship et al., 2006; Mason et al., 2013). Indeed, N-cadherin and/or Shroom3 downregulation expands the apical cell surface, producing a loss of apical F-actin and a failure of NT closing, reinforcing the role of N-cadherin in apical constriction (Morita et al., 2010; Nandadasa et al., 2009; Plageman et al., 2011). Vangl2 directly controls N-cadherin expression (Nagaoka et al., 2014) and, thus, we propose that rosette formation is part of the general shaping of the PNP. This requires a continuous network of tight and adherens junctions, and it is impaired in *Vangl2*$^{+/Lp}$ embryos or upon exposure to CytD and Y-27632, which significantly impair rosette formation.

As we show here, apical actin cables represent another planar polarised epithelial structure that forms in the most anterior part of the PNP. Mediolaterally oriented apical actomyosin cables, regulated by the Wnt-PCP pathway, are thought to be crucial for the polarised bending of the pre-elevated cranial NP, and therefore for NT closure by inflection (McGreevy et al., 2015; Nishimura et al., 2012). We also observed these cell arrangements in the anterior PNP, in association with zipping but oriented in an anteroposterior direction, highlighting the difference between the mechanisms driving cranial and caudal NT closure. Thus, although the caudal epiblast cells rely on actomyosin apical pulse contraction to initiate PNP folding, cells interact more intensely at more anterior positions. There they form more rosettes and establish planar polarised cell alignments under the control of Wnt-PCP signalling, highlighting the complexity involved in shaping the anterior part of the PNP prior to closure.

Development (2018) 145, dev157487. doi:10.1242/dev.157487

Actin disorganisation provokes an abnormal increase in the apical cell surface area affecting the general morphology of the neural folds

The NP contacts the surface ectoderm dorsally, the paraxial mesoderm laterally and the notochord ventrally. Both the surface ectoderm and notochord are required to induce dorsal and midline bending of the NP (DLHPs and MHP, respectively), points that drive neural fold closing (Ybot-Gonzalez et al., 2002, 2007a). Here, we show that atypical bending of the lateral neural fold in *Vangl2*$^{+/Lp}$ embryos is phenocopied by chemically inhibiting actin dynamics, demonstrating that correct apical F-actin assembly is needed to shape the neural fold and to provide it with the structural rigidity required for elevation. These alterations in *Vangl2*$^{+/Lp}$ embryos seem to affect the entire NP, e.g. the increased apical cell area or the less intense actin cumuli. However, rosette formation and polarised cell alignment are distorted in the straight part of the neural fold, juxtaposed to the paraxial mesoderm. Hence, contacts with the surface ectoderm dorsally and notochord ventral, might prevent these regions from becoming morphologically affected by the alterations to the actin cytoskeleton. Indeed, at early stages when the DLHP is absent, the outward flexure of the entire lateral fold is affected in *Vangl2*$^{+/Lp}$ embryos, and following exposure to CytD at a later stage, when the MHP is absent, the dorsal part of the neural fold remains unaffected (Ybot-Gonzalez and Copp, 1999; this work). Moreover, the increase in the apical cell area in the PNT and NSB/CLE occurs at a similar rate in *Vangl2*$^{+/Lp}$ and *Vangl2*$^{+/+}$ embryos, strengthening the idea of a general rather than a more regionalised process. The mutation of genes that affect F-actin reorganisation and that impede cranial NT closure, such as *Shroom3* and cofilin 1, also provokes an expansion of the apical cell area, producing a thinner NP and outward flexure of the cranial neural folds (Grego-Bessa et al., 2015; Hildebrand and Soriano, 1999; McGreevy et al., 2015). Thus, we predict that Wnt-PCP signalling organises the apical F-actin throughout the PNP, which together with myosin drives NP folding by apical contraction. In more anterior parts of the PNP, the Wnt-PCP pathway produces cellular rearrangements through F-actin, providing the neural folds with a rigid apical structure that can withstand the external forces required for their elevation. Disruption of the Wnt-PCP pathway increases the apical cell area, provoking a loss of apical rigidity that affects neural fold morphology, reducing the apico-basal width and increasing its length. These morphological changes induce aberrant bending, causing the separation of the dorsal tips of the neural folds and impeding correct NT closure, resulting in spina bifida.

Altered apico-basal polarity in the early epiblast by Wnt-PCP signalling could affect NSB/CLE cells in the caudal PNP

The PNP contains cells at different stages of specification and differentiation; caudal neural cell progenitors are initially found in the caudal NSB/CLE zone (as bipotent NMPs), then, as the axis elongates, they occupy more anterior positions in the PNT and differentiate further. Here, we show that the NMPs in the NSB/CLE of *Vangl2*$^{+/Lp}$ embryos have a larger apical area than those in the wild type, a phenotype apparently arising from a primary defect in germ layer morphogenesis. This observation is consistent with the Wnt-PCP pathway and Vangl2 being required for the formation of the epiblast and primitive streak (Tao et al., 2009).

NMPs are first detected in the epiblast at E7.5, close to the border between the node and primitive streak. NMPs persist in the chordoneural hinge (CNH) and its surrounding areas during trunk and tail formation, peaking at E9.5 and decreasing thereafter until they are undetectable by E14.5 (Wymeersch et al., 2016). The epiblast is disorganised and primitive streak formation defective in dual *mpk1*$^{+/-}$ (*Prickle1*$^{+/-}$) and *Vangl2*$^{+/Lp}$ heterozygous mutants, in association with abnormal cell morphology, disorganised actin and the loss of apico-basal polarity (Suriben et al., 2009; Tao et al., 2009). Hence, Vangl2 is needed to establish/maintain apico-basal polarity and for cytoskeletal reorganisation at early stages of development. We postulate that the same phenomenon occurs later in development, but as the phenotype is milder at early stages, the direct consequences of these alterations can be studied. Altered apico-basal polarity in the epiblast resulting from perturbations in the Wnt-PCP pathway affects the NSB/CLE cells in the caudal PNP, which acquire a notably larger apical domain. This phenotype is inherited by all their descendants, including the NMPs and the neural cells incorporated into the neural folds.

Here, weaker Vangl2 activity in the giant cells disrupts the balance of cell fates, increasing neural fates and reduction of NMPs in the PNT. Hence, Vangl2 appears to influence NMP differentiation into neural cells rather than NMP specification. Nkd1 expression is upregulated in mice with mutations in Cdx2, a protein that inhibits Dishevelled, which is in turn needed for NT closure via Wnt-PCP signalling (van de Ven et al., 2011). Downregulation of Cdx2, or Wnt3a, dampens canonical Wnt signalling and favours a neural fate (Takada et al., 1994); the Wnt-PCP pathway might also be impaired in these mutants affecting PNP cell fate as suggested here. Further studies will be necessary to gain a more complete picture of how the Wnt-PCP pathway participates in such events.

MATERIALS AND METHODS

Animals

The *Daam1* gene trap mutant mice were obtained from Baygenomics (RRT390; Li et al., 2011) and they were maintained on a C57 background. The loop-tail (*Vangl2*^{Lp}) inbred strain carrying the *Vangl2* mutation was originally obtained from Jackson Laboratories and it was maintained on a CBA background. Mutant mice exhibit neurodevelopmental defects leading to short, curly tails and occasionally spina bifida. *Daam1*$^{+/gt}$ mice were crossed with the *Vangl2*$^{+/Lp}$ mice to produce double heterozygote *Vangl2*$^{+/Lp}$/*Daam1*$^{+/gt}$ mice. After overnight mating, *Vangl2*$^{+/Lp}$ and *Daam1*$^{+/gt}$ pairs were checked for vaginal plugs and the day on which a copulation plug was found was designated as E0.5. The mice were maintained on a 12-h light/dark cycle (lights on from 08:00 to 20:00), and they had *ad libitum* access to food (Global Diet 2014 S, Harlan-Teklad) and water. All procedures involving experimental animals were performed in compliance with local, national and European animal welfare laws, guidelines and policies.

Embryo extraction, culture and genotyping

Embryos were collected at stage E10.5-E12 and their yolk sacs were used for *Vangl2* and *Daam1* genotyping as described previously (Li et al., 2011; Stanier et al., 1995). Embryos were cultured for 6 h at 37°C (Copp et al., 2000) in the presence of cytochalasin D (CytD, 0.05 µg/ml) dissolved in DMSO (Ybot-Gonzalez and Copp, 1999) or Y-27632 (10 µM) dissolved in sterile distilled water (Ybot-Gonzalez et al., 2007b). In each experiment control, embryos were cultured in the presence of the vehicle alone. After culture, the embryos were assessed for yolk sac circulation and presence of heartbeat, and only healthy embryos were used in the experiments. Embryos were analysed for external malformations and fixed in 4% paraformaldehyde (PFA) in PBS for *in situ* hybridisation, or Haematoxylin and Eosin (H&E) and phalloidin staining (P1951-1MG, diluted 1:500 in PBS; Sigma). At least three embryos were analysed for each condition.

In situ hybridisation

Whole-mount *in situ* hybridisation was carried out using sense and antisense digoxigenin-labelled riboprobes prepared using a digoxigenin RNA labelling kit (Roche) according to the manufacturer's instructions. As

Development (2018) 145, dev157487. doi:10.1242/dev.157487

described previously (Ybot-Gonzalez et al., 2005) E9.5 (25-30 somite) mouse embryos were analysed with the probes for: *Wnt5a* (Gavin et al., 1990), *Wnt3a* (Roelink and Nusse, 1991), *Daam1* (Ybot-Gonzalez et al., 2007b), *Vangl2* (Doudney et al., 2005), *Prickle1* (Crompton et al., 2007), *Gpc4* (Ybot-Gonzalez et al., 2005), *RhoA* (Ybot-Gonzalez et al., 2007b) and *Ptk7* (Paudyal et al., 2010). A cDNA probe for *Shroom3* was generated using the primers 5′-AGAACTTGGAGGAGCCTAGC-3′ and 5′-TGCATCATGCTGACATCAGG-3′, which amplify a 519 bp region between nucleotides 246 and 765 (GenBank accession no. NM_015756.2). Whole embryos were photographed on a stereomicroscope (SteREO Discovery V8 with AxioCam Erc8, Zeiss) and 50-µm-thick vibratome sections on an Olympus BX-61 photomicroscope. Sense-strand riboprobes were used as controls for specificity and produced no specific signal. At least three embryos were analysed for each probe.

Quantitative RT-PCR

The expression of genes in the Wnt-PCP pathway was analysed by quantitative RT-PCR. *Vangl2*$^{+/+}$ and *Vangl2*$^{+/Lp}$ embryos at developmental stage E9.5 were preserved in RNA-later (Ambion) until total RNA was extracted with the TRIsure reagent (Bioline) according to the manufacturer's recommendations. The PrimeScript RT Master Mix (Perfect Real Time Kit, Takara Bio) was used for RT-PCR using the ViiA7 Real-Time PCR system (Applied Biosystems). The primers used are described in Table S5. *Gapdh* was the housekeeping gene used, and the reactions were run in triplicate and repeated on several independent samples for each genotype. The fold change in gene expression was determined using the Ct method (Livak and Schmittgen, 2001), normalising expression to the housekeeping target gene. Fold changes in the range of −1.5 and 1.5 were not considered different. Three whole *Vangl2*$^{+/+}$ and *3 Vangl2*$^{+/Lp}$ embryos were analysed.

General morphology, and histological analysis of embryos and foetuses

Foetuses obtained between E11.5 and E17.5 were analysed for external malformations and photographed on a stereomicroscope (SteREO Discovery V8 with AxioCam Erc8, Zeiss) prior to fixing in 4% PFA. The embryos were stored in 70% ethanol and then embedded in paraffin wax to obtain transverse sections (7 µm thick). The sections were stained with Ehrlich H&E, and representative sections were selected from at least three serially sectioned embryos for each condition and photographed on an Olympus BX-61 photomicroscope. At least three embryos for each condition were analysed.

Immunohistochemistry

Sections of E9.5 embryos were embedded in gelatine (15% sucrose and 7.5% gelatine in PBS) for immunohistochemical analysis and cryosections containing the area of interest were obtained (10 and 50 µm thick) on a Leica CM1950 cryostat. Sections were processed for each primary antibody against β-catenin, ZO1 or N-cadherin as described previously (López-Escobar et al., 2015), and they were then incubated with the appropriate secondary antibody (see Table S6). Phalloidin-tetramethylrhodamine B isothiocyanate was used to localise F-actin (P1951, Sigma-Aldrich), diluted 1:500 in PBT (PBS and 0.1% triton). Sections were protected with Hydromount (HS-106, National Diagnostics); 10-µm-thick sections were photographed on an Olympus BX61 microscope and the 50-µm-thick sections were analysed by confocal microscopy (TCS-SP2-AOBS, Leica).

Whole-mount E9.5 embryos were fixed using an optimised protocol for each immunolabelling experiment. To compare between the different conditions, embryos for each experiment were kept all together in a tube throughout the entire procedure only separating them for confocal microscopy. One group of embryos was fixed with Dent's fixative and stored in 100% methanol for H3 and ZO1 immunohistochemistry. The other group of embryos was fixed in 4% PFA and stored in 100% methanol for Sox2, T and ZO1 triple immunohistochemistry. Finally, another group of embryos were fixed in 4% PFA overnight for phalloidin and MHC-IIB. For immunolabelling, the embryos were processed as described elsewhere (McGreevy et al., 2015). The primary and secondary antibodies used are described in Table S6. The PNP was dissected out, opening the NT to facilitate flattening and analysed as whole mounts with Hydromount on a Nikon A1 confocal microscope. For ZO1 staining, a *z*-series (0.95 µm steps) was collected using a 20× glycerol-objective in a 2048×2048 format, applying a zoom of 1.664. For the triple immunohistochemistry, *z*-series (0.925 µm steps for ZO1 and 3 µm steps for Sox2 and T) were acquired using a 20× glycerol-objective in a 2048×2048 format, applying a zoom of 1.462. For phalloidin and MHC-IIB or p-MLC immunohistochemistry, *z*-series (0.925 µm steps) were acquired using a 20× glycerol-objective in a 2048×2048 format, applying a zoom of 1.462. At least three different embryos were processed for each primary antibody or phalloidin.

Analysis of the length and apico-basal width of the neural folds

The apico-basal width of the transverse section of the neural folds was quantified by measuring the length of drawn lines using ImageJ. For each neural fold, two levels of the apico-basal width within the region juxtaposed to the paraxial mesoderm were measured (straight region of the neural fold marked with two asterisks in Fig. 1A): the most dorsal width (Fig. S3, 'd') and the most ventral width (Fig. S3, 'v'). Furthermore, the total neural fold length was measured in both genotypes by drawing a line along the apical side of the straight region of the neural fold using ImageJ (Fig. S3, dotted line). We calculated the ratio between the length (L) and the apico-basal ventral width (v) of the neural fold analysing each section individually. The data were obtained from both neural folds of eight embryos for each genotype (16 neural folds/condition) and statistical significance was determined by Student's *t*-test.

Analysis of the bending and apical surface eversion of the neural folds

The degree of bending of individual neural folds was measured by applying the angle function in ImageJ to sections of the PNP. The angles were taken from the line that joins the lumen side of the MHP and the DLHP and that which joins the lumen side of the MHP and the most outward flexure of the neural fold (see Fig. S3). Statistical significance was determined by Student's *t*-test using the following samples: 14 *Vangl2*$^{+/+}$ neural folds; 20 *Vangl2*$^{+/Lp}$ neural folds; 14 *Vangl2*$^{+/+}$ neural folds treated with cytochalasin D; 10 *Vangl2*$^{+/+}$ neural folds treated with Y-27632.

Quantification of the apical cell arrangements at the lateral neural fold

To evaluate the apical cell arrangement, the neuropore was tilted manually as it was lowered into the gelatine, exposing a flat vision of the inner side of the anterior neural fold to the closing point of the NT. Sections of the elevating neural folds (50 µm thick) were immunolabelled for ZO1. To improve the visualisation of the flat apical sides of the cells in the neural fold after immunolabelling, 3D images were obtained from *z*-stacks of confocal images using ImageJ. The apical cell area was measured using ImageJ. Samples used were: 4 *Vangl2*$^{+/+}$ embryos and 140 cells analysed; 5 *Vangl2*$^{+/Lp}$ embryos and 165 cells analysed; 3 *Vangl*$^{Lp/Lp}$ embryos and 127 cells analysed; 3 *Vangl2*$^{+/+}$ embryos treated with CytD and 125 cells analysed; 2 *Vangl2*$^{+/Lp}$ embryos treated with CytD and 116 cells analysed; 3 *Vangl2*$^{+/+}$ embryos treated with Y-27632 and 127 cells analysed; 3 *Vangl2*$^{+/Lp}$ embryos treated with Y-27632 and 109 cells analysed (2-3 sections of each embryo analysed). Global comparisons of the cellular apical area were evaluated using an ANOVA test with Welch's correction, and multiple comparisons were analysed using the post-hoc Games-Howell test. Individual comparisons of the apical cell area in the PNT of *Vangl2*$^{+/Lp}$ and after each treatment of *Vangl2*$^{+/+}$ embryos were evaluated with a Mann–Whitney U test.

Analysis of actin and myosin planar distribution

E9.5 mouse embryos were fixed in 4% PFA and stained with phalloidin, and antibodies against MHC-IIB and p-MLC. The maximal projections of confocal images from a flat-mounted PNP were obtained using a Nikon A1 confocal microscope. All images were obtained using the same parameters.

Analysis of actin intensity

A region of interest (ROI) of 200×200 pixels was selected to obtain the intensity histograms of phalloidin labelling from the PNT of *Vangl2*$^{+/+}$ and *Vangl2*$^{+/Lp}$ embryos using ImageJ. One ROI was used per embryo (3 *Vangl2*$^{+/+}$ and 5 *Vangl2*$^{+/Lp}$) and 40,000 pixels were analysed per ROI.

Development (2018) 145, dev157487. doi:10.1242/dev.157487

Mann–Whitney U test was used to compare mean intensity values, and Pearson's Chi-squared test to compare the proportion of pixels with the maximum intensity value between the two genotypes.

Analysis of actin cable orientation in aligned cell rearrangements

An ROI that covered the most anterior part of the NP (PNT) was outlined using ImageJ (540×400 pixels). Actin cables joining five to nine aligned cells were counted and their orientation was measured relative to the mediolateral axis of the embryo. The angular distribution was plotted in a histogram representing two groups: lines with angles from 0° to 45° (mediolateral orientation) and lines with angles from 45° to 90° (anterior-posterior orientation; see Fig. 2O,P). One ROI was used per embryo (5 *Vangl2*$^{+/+}$ and 11 *Vangl2*$^{+/Lp}$). Student's *t*-test was used to compare the number of actin cells alignments, and Fisher's exact test to compare the proportions of cell alignment orientations.

Analysis of actin cumulus and basal intensity

ROIs (100×100 pixels) were selected in the PNT of embryos: ten basal and ten cumuli intensity plot profiles were obtained along the linear boundary of two neighbouring cells (basal) and along cumuli using the ImageJ function 'Plot Profile'. The distribution of the total fluorescence intensity within the ROI was measured using the histogram function of ImageJ (Fig. S5A,a,a′ and Fig. S5B,b,b′). Ten measurements/ROIs were used for each profile; two different ROIs per embryo from 3 *Vangl2*$^{+/+}$ and 3 *Vangl2*$^{+/Lp}$ embryos. Student's *t*-test was used to determine statistical significance.

Quantification of apical cumulus of actin

An ROI of 100×100 pixels in the PNT and the NSB/CLE regions were selected using ImageJ. The number of actin cumuli in those areas was determined using the 'multi-point' tool in ImageJ and the average number of cumuli in each area and genotype was compared (Fig. 2Oi,Oii,V). One ROI was used per embryo (5 *Vangl2*$^{+/+}$ and 8 *Vangl2*$^{+/Lp}$). Student's *t*-test was used to determine statistical significance.

Analysis of paired cumuli of p-MLC in neighbouring cells (dense supracellular structures)

ROIs of 200×200 pixels were analysed to determine the number of paired p-MLC cumuli. Three ROIs were used per embryo (3 *Vangl2*$^{+/+}$ and 3 *Vangl2*$^{+/Lp}$).

The distance between the paired cumuli was measured using ImageJ. Samples used were 188 cumuli from 3 *Vangl2*$^{+/+}$ and 248 cumuli from 3 *Vangl2*$^{+/Lp}$ embryos. Student's *t*-test was used to determine statistical significance.

Analysis of the myosin distribution

The presence of MHC-IIB was analysed in segmented images (see below) of the ZO1 immunolabelled PNP from embryos. The cell population in the PNP was divided into small (apical cell area <13 µm^2) and giant cells (apical cell area >13 µm^2). The number of cells with MHC-IIB was determined using the 'multi-point' tool in ImageJ. For giant cells, >50 cells/embryo were analysed from 3 embryos of each genotype; for small cells, >600 cells/embryo from 3 embryos per genotype were analysed. Pearson's Chi-squared test was used to determine statistical significance.

Cell dynamics

Using the semi-automated image-segmenting program Seedwater Segmenter (Mashburn et al., 2012), confocal ZO1-stained images from flatted PNP were segmented to produce separate ROIs for each cell. The segmented images were treated as the whole PNP, and they were also divided into neural tube (NT), pre-neural tube (PNT, which included two peripheral zones and a central zone) and the node-streak border/caudal lateral epiblast (NSB/CLE), as described previously (Henrique et al., 2015). The rectangle chosen to define each ROI was of similar dimensions, measured in ImageJ (400×600 pixels). The apical area of the cell was determined using ImageJ and a custom image analysis tool (McGreevy et al., 2015).

The same macro was also used to determine the presence of rosettes and their complexity (number of cells with a vertex forming a rosette). In order to calculate vertex complexity (i.e. the number of cells at a shared junction), we used custom ImageJ macros to extract individual vertices from the segmented output produced by SeedWater Segmenter. The Segmenter algorithm produces an indexed image in which each cell has been identified and its area filled with a unique identifying integer as its intensity. To detect shared junctions between cells, we centred a circle with a user-defined radius at each pixel within the indexed image (McGreevy et al., 2015). We then counted the number of unique integer intensities detected within the circle. When three or more intensities were detected, the centre pixel of the circle was filled in on a blank image. After the circle had been passed over the entire image, the blank image contained a cluster of filled-in pixels corresponding to each vertex. We ran the 'Find Particles' function on this image to extract individual 'vertex' ROIs for each vertex pixel cluster. To find the order of these vertex pixel clusters, we used the original indexed image to detect the number of unique intensities appearing within each vertex ROI. Cells were colour-coded based on their coordination number using another custom macro and the percentage of cells in each bin was plotted. The average number of cells counted in each experiment was: *Vangl2*$^{+/+}$ embryos (n=6), NT area 250 cells/embryo, PNT area 1200 cells/embryo, NSB/CLE area 344 cells/embryo; *Vangl2*$^{+/Lp}$ embryos (n=4), NT area 482 cells/embryo, PNT area 1250 cells/embryo, NSB/CLE area 240 cells/embryo; *Vangl2*$^{+/+}$ embryos treated with CytD (n=4), PNT area 1256 cells/embryo, NSB/CLE area 360 cells/embryo; *Vangl2*$^{+/+}$ embryos treated with Y-27623 (n=4), PNT area 1216 cells/embryo, NSB/CLE area 456 cells/embryo. Cells with an apical area greater than 13 µm were considered 'giant cells' and those smaller than 13 µm 'small cells'. For the triple immunohistochemistry (ZO1, Sox2 and T), 318 cells/embryo from 4 *Vangl2*$^{+/+}$ embryos and 385 cells/embryo from 4 *Vangl2*$^{+/Lp}$ embryos were analysed and for the giant cell population 45 cells/embryo and 144 cells/embryo from 4 *Vangl2*$^{+/+}$ and 4 *Vangl2*$^{+/Lp}$ embryos were analysed, respectively. The percentage of cells with a vertex forming a rosette, the rosette order, number of giant cells and analysis of T and Sox2 expression in giant cells were compared using a proportion comparison test, Pearson's Chi-squared test. Comparisons of the apical cell area were calculated using the Mann–Whitney U test. Global comparison of the apical cell area of the NMPs (T$^+$/Sox2$^+$) vs the mesodermal (T$^+$/Sox2$^-$) or neural cell fates (T$^-$/Sox2$^+$) for each genotype was analysed using an ANOVA test with Welch's correction, and multiple comparisons were analysed using the post-hoc Games-Howell test (P<0.05).

Statistical analysis

Global comparisons of the cellular apical area were evaluated using an ANOVA test with Welch's correction, and multiple comparisons were analysed using the post-hoc Games-Howell test (IBM SPSS Statistics 19 software).

To estimate the difference between proportions obtained from independent samples of two populations we used the Pearson Chi-squared test. In the 2×2 table study we also obtained the odds ratio (OR) and the 95% confidence interval. We used OpenEpi software (www.OpenEpi.com; updated 06/04/2013, accessed 01/03/2018). For the small sample size proportion studies, we used Fisher's exact test in OpenEpi software.

The means of two populations obtained from independent samples were compared either with a Student's *t*-test when the data followed a normal distribution or a non-parametric Mann–Whitney U test when the data did not follow a normal distribution. For these analyses, we used Epidat software (http://www.sergas.es/Saude-publica/EPIDAT; version 4.2, July 2016) and IBM SPSS Statistics 19 software.

The effect size d of Cohen and the confidence interval were calculated using 'Calculation of Effect Sizes' (http://www.psychometrica.de/effect_size.html; Lenhard and Lenhard, 2016). The power of the studies was calculated using Epidat software and in all statistical studies differences were considered to be statistically significant at P<0.05.

Acknowledgements

We are very thankful to Jose Ramón Martínez-Morales, Solveig Thorsteinsdottir, David Cano and Andrew J. Copp for valuable advice and comments on the manuscript. We thank Tristan Rodriguez, Jennifer Murdoch, Roel Nusse and Andrew McMahon for generously providing us with mouse cDNA plasmids of *Prickle1*, *Ptk7*, *Wnt3a* and *Wnt5a*, respectively. We also gratefully acknowledge Patricia Fernandez del Valle and Juan Manuel Praena for their invaluable advice

with the statistical analysis, Konstantin Levitskiy for helping with the confocal microscopy images, and Mark Sefton and Arturo Amarilla for revising the manuscript.

Competing interests
The authors declare no competing or financial interests.

Author contributions
Conceptualization: P.Y.-G., B.L.-E., J.M.C.-V., R.C.M., J.M.-R.; Methodology: P.Y.-G., B.L.-E., J.M.C.-V., R.C.M., D.S., D.S.V., T.F.P., J.A.S.-A. L.A.D.; Software: P.Y.-G., B.L.-E., J.M.C.-V., D.S.V., L.A.D.; Validation: P.Y.-G., B.L.-E., J.M.C.-V., J.A.S.-A.; D.S.V., T.F.P., L.A.D.; Formal analysis: P.Y.-G., B.L.-E., J.M.C.-V., D.S.V., J.A.S.-A., R.C.M., D.S.; Investigation: P.Y.-G., B.L.-E., J.M.C.-V., R.C.M., J.A.S.-A., D.S., Resources: P.Y.-G., B.L.-E., J.M.C.-V., D.S.V., T.F.P., J.A.S.-A., D.S., J.M.-R. L.A.D.; Data curation: P.Y.-G., B.L.-E., J.M.C.-V.; Writing - original draft: P.Y.-G., B.L.-E., J.M.C.-V.; Writing -review & editing: P.Y.-G., J.A.S.-A. J.M.-R., D.S.V., T.F.P., L.A.D.; Visualization: P.Y.-G., B.L.-E., J.M.C.-V.; Supervision: P.Y.-G., L.A.D.; Project administration: P.Y.-G.; Funding acquisition: P.Y.-G., J.M.-R.

Funding
This work was supported by grants from the Instituto de Salud Carlos III (PS09/00050, CP08/00111, CPII14/00033, PI14/01075 and PI17/00693 to P.Y.-G.) co-financed by the European Regional Development Fund “A way to achieve Europe”; the Andalusian Health Service, Junta de Andalucia (Servicio Andaluz de Salud, Junta de Andalucia; PI-0438-2010 to P.Y.-G.); the Andalusian Regional Ministry of Economy, Science and Innovation (Consejería de Economía, Innovaciόń, Ciencia y Empleo, Junta de Andalucíá; P11-cts-7634 to P.Y.-G.); the National Institutes of Health (R01 HD044750 to L.A.D.); and the National Science Foundation (CMMI-1100515 to L.A.D.). In addition, D.S.V. was supported by the “Biomechanics in Regeneration” Training Program from the National Institute of Biomedical Imaging and Bioengineering (BiRM T32 EB003392). Deposited in PMC for release after 12 months.

Supplementary information
Supplementary information available online at
http://dev.biologists.org/lookup/doi/10.1242/dev.157487.supplemental

References
Andersson, E. R., Bryjova, L., Biris, K., Yamaguchi, T. P., Arenas, E. and Bryja, V. (2010). Genetic interaction between Lrp6 and Wnt5a during mouse development. *Dev. Dyn.* **239**, 237-245.

Blankenship, J. T., Backovic, S. T., Sanny, J. S. P., Weitz, O. and Zallen, J. A. (2006). Multicellular rosette formation links planar cell polarity to tissue morphogenesis. *Dev. Cell* **11**, 459-470.

Brouns, M. R., Matheson, S. F., Hu, K. Q., Delalle, I., Caviness, V. S., Silver, J., Bronson, R. T. and Settleman, J. (2000). The adhesion signaling molecule p190 RhoGAP is required for morphogenetic processes in neural development. *Development* **127**, 4891-4903.

Copp, A. J., Checiu, I. and Henson, J. N. (1994). Developmental basis of severe neural tube defects in the loop-tail (Lp) mutant mouse: use of microsatellite DNA markers to identify embryonic genotype. *Dev. Biol.* **165**, 20-29.

Copp, A., Cogram, P., Fleming, A., Gerrelli, D., Henderson, D., Hynes, A., Kolatsi-Joannou, M., Murdoch, J. and Ybot-Gonzalez, P. (2000). Neurulation and neural tube closure defects. *Methods Mol. Biol.* **136**, 135-160.

Crompton, L. A., Du Roure, C. and Rodriguez, T. A. (2007). Early embryonic expression patterns of the mouse Flamingo and Prickle orthologues. *Dev. Dyn.* **236**, 3137-3143.

Doudney, K., Ybot-Gonzalez, P., Paternotte, C., Stevenson, R. E., Greene, N. D., Moore, G. E., Copp, A. J. and Stanier, P. (2005). Analysis of the planar cell polarity gene Vangl2 and its co-expressed paralogue Vangl1 in neural tube defect patients. *Am. J. Med. Genet. A* **136**, 90-92.

Escuin, S., Vernay, B., Savery, D., Gurniak, C. B., Witke, W., Greene, N. D. and Copp, A. J. (2015). Rho-kinase-dependent actin turnover and actomyosin disassembly are necessary for mouse spinal neural tube closure. *J. Cell Sci.* **128**, 2468-2481.

Etienne-Manneville, S. and Hall, A. (2002). Rho GTPases in cell biology. *Nature* **420**, 629-635.

Fletcher, A. G., Osterfield, M., Baker, R. E. and Shvartsman, S. Y. (2014). Vertex models of epithelial morphogenesis. *Biophys. J.* **106**, 2291-2304.

Galea, G. L., Cho, Y. J., Galea, G., Mole, M. A., Rolo, A., Savery, D., Moulding, D., Culshaw, L. H., Nikolopoulou, E., Greene, N. D. E. et al. (2017). Biomechanical coupling facilitates spinal neural tube closure in mouse embryos. *Proc. Natl. Acad. Sci. USA* **114**, E5177-E5186.

Garriock, R. J., Chalamalasetty, R. B., Kennedy, M. W., Canizales, L. C., Lewandoski, M. and Yamaguchi, T. P. (2015). Lineage tracing of neuromesodermal progenitors reveals novel Wnt-dependent roles in trunk progenitor cell maintenance and differentiation. *Development* **142**, 1628-1638.

Gavin, B. J., McMahon, J. A. and McMahon, A. P. (1990). Expression of multiple novel Wnt-1/int-1-related genes during fetal and adult mouse development. *Genes Dev.* **4**, 2319-2332.

Goto, T. and Keller, R. (2002). The planar cell polarity gene strabismus regulates convergence and extension and neural fold closure in Xenopus. *Dev. Biol.* **247**, 165-181.

Grego-Bessa, J., Hildebrand, J. and Anderson, K. V. (2015). Morphogenesis of the mouse neural plate depends on distinct roles of cofilin 1 in apical and basal epithelial domains. *Development* **142**, 1305-1314.

Habas, R., Kato, Y. and He, X. (2001). Wnt/Frizzled activation of Rho regulates vertebrate gastrulation and requires a novel Formin homology protein Daam1. *Cell* **107**, 843-854.

Habas, R., Dawid, I. B. and He, X. (2003). Coactivation of Rac and Rho by Wnt/Frizzled signaling is required for vertebrate gastrulation. *Genes Dev.* **17**, 295-309.

Harding, M. J., McGraw, H. F. and Nechiporuk, A. (2014). The roles and regulation of multicellular rosette structures during morphogenesis. *Development* **141**, 2549-2558.

Henrique, D., Abranches, E., Verrier, L. and Storey, K. G. (2015). Neuromesodermal progenitors and the making of the spinal cord. *Development* **142**, 2864-2875.

Hildebrand, J. D. and Soriano, P. (1999). Shroom, a PDZ domain-containing actin-binding protein, is required for neural tube morphogenesis in mice. *Cell* **99**, 485-497.

Keller, R. (2002). Shaping the vertebrate body plan by polarized embryonic cell movements. *Science* **298**, 1950-1954.

Kim, H. Y. and Davidson, L. A. (2011). Punctuated actin contractions during convergent extension and their permissive regulation by the non-canonical Wnt-signaling pathway. *J. Cell Sci.* **124**, 635-646.

Kinoshita, N., Sasai, N., Misaki, K. and Yonemura, S. (2008). Apical accumulation of Rho in the neural plate is important for neural plate cell shape change and neural tube formation. *Mol. Biol. Cell* **19**, 2289-2299.

Lenhard, W. and Lenhard, A. (2016). Calculation of Effect Sizes. Available: http://www.psychometrica.de/effect_size.html. Dettelbach (Germany): Psychometrica.

Li, D., Hallett, M. A., Zhu, W., Rubart, M., Liu, Y., Yang, Z., Chen, H., Haneline, L. S., Chan, R. J., Schwartz, R. J. et al. (2011). Dishevelled-associated activator of morphogenesis 1 (Daam1) is required for heart morphogenesis. *Development* **138**, 303-315.

Lienkamp, S. S., Liu, K., Karner, C. M., Carroll, T. J., Ronneberger, O., Wallingford, J. B. and Walz, G. (2012). Vertebrate kidney tubules elongate using a planar cell polarity-dependent, rosette-based mechanism of convergent extension. *Nat. Genet.* **44**, 1382-1387.

Livak, K. J. and Schmittgen, T. D. (2001). Analysis of relative gene expression data using real-time quantitative PCR and the 2−ΔΔCT Method. *Methods* **25**, 402-408.

López-Escobar, B., Cano, D. A., Rojas, A., de Felipe, B., Palma, F., Sánchez-Alcázar, J. A., Henderson, D. and Ybot-González, P. (2015). The effect of maternal diabetes on the Wnt-PCP pathway during embryogenesis as reflected in the developing mouse eye. *Dis. Model. Mech.* **8**, 157-168.

Maekawa, M., Ishizaki, T., Boku, S., Watanabe, N., Fujita, A., Iwamatsu, A., Obinata, T., Ohashi, K., Mizuno, K. and Narumiya, S. (1999). Signaling from Rho to the actin cytoskeleton through protein kinases ROCK and LIM-kinase. *Science* **285**, 895-898.

Mahaffey, J. P., Grego-Bessa, J., Liem, K. F., Jr and Anderson, K. V. (2013). Cofilin and Vangl2 cooperate in the initiation of planar cell polarity in the mouse embryo. *Development* **140**, 1262-1271.

Martin, A. C., Kaschube, M. and Wieschaus, E. F. (2009). Pulsed contractions of an actin-myosin network drive apical constriction. *Nature* **457**, 495-499.

Mashburn, D. N., Lynch, H. E., Ma, X. and Hutson, M. S. (2012). Enabling user-guided segmentation and tracking of surface-labeled cells in time-lapse image sets of living tissues. *Cytometry Part A* **81A**, 409-418.

Mason, F. M., Tworoger, M. and Martin, A. C. (2013). Apical domain polarization localizes actin-myosin activity to drive ratchet-like apical constriction. *Nat. Cell Biol.* **15**, 926-936.

Massarwa, R. and Niswander, L. (2013). In toto live imaging of mouse morphogenesis and new insights into neural tube closure. *Development* **140**, 226-236.

McGreevy, E. M., Vijayraghavan, D., Davidson, L. A. and Hildebrand, J. D. (2015). Shroom3 functions downstream of planar cell polarity to regulate myosin II distribution and cellular organization during neural tube closure. *Biol Open* **4**, 186-196.

Morita, H., Nandadasa, S., Yamamoto, T. S., Terasaka-Iioka, C., Wylie, C. and Ueno, N. (2010). Nectin-2 and N-cadherin interact through extracellular domains and induce apical accumulation of F-actin in apical constriction of Xenopus neural tube morphogenesis. *Development* **137**, 1315-1325.

Nagaoka, T., Ohashi, R., Inutsuka, A., Sakai, S., Fujisawa, N., Yokoyama, M., Huang, Y. H., Igarashi, M. and Kishi, M. (2014). The Wnt/planar cell polarity pathway component Vangl2 induces synapse formation through direct control of N-cadherin. *Cell Rep.* **6**, 916-927.

Nandadasa, S., Tao, Q., Menon, N. R., Heasman, J. and Wylie, C. (2009). N- and E-cadherins in Xenopus are specifically required in the neural and non-neural

ectoderm, respectively, for F-actin assembly and morphogenetic movements. *Development* **136**, 1327-1338.

Nikolopoulou, E., Galea, G. L., Rolo, A., Greene, N. D. E. and Copp, A. J. (2017). Neural tube closure: cellular, molecular and biomechanical mechanisms. *Development* **144**, 552-566.

Nishimura, T. and Takeichi, M. (2009). Remodeling of the adherens junctions during morphogenesis. *Curr. Top. Dev. Biol.* **89**, 33-54.

Nishimura, T., Honda, H. and Takeichi, M. (2012). Planar cell polarity links axes of spatial dynamics in neural-tube closure. *Cell* **149**, 1084-1097.

Ossipova, O., Kim, K. and Sokol, S. Y. (2015). Planar polarization of Vangl2 in the vertebrate neural plate is controlled by Wnt and Myosin II signaling. *Biol Open* **4**, 722-730.

Paudyal, A., Damrau, C., Patterson, V. L., Ermakov, A., Formstone, C., Lalanne, Z., Wells, S., Lu, X., Norris, D. P., Dean, C. H. et al. (2010). The novel mouse mutant, chuzhoi, has disruption of Ptk7 protein and exhibits defects in neural tube, heart and lung development and abnormal planar cell polarity in the ear. *BMC Dev. Biol.* **10**, 87.

Pinson, K. I., Brennan, J., Monkley, S., Avery, B. J. and Skarnes, W. C. (2000). An LDL-receptor-related protein mediates Wnt signalling in mice. *Nature* **407**, 535-538.

Plageman, T. F., Jr, Zacharias, A. L., Gage, P. J. and Lang, R. A. (2011). Shroom3 and a Pitx2-N-cadherin pathway function cooperatively to generate asymmetric cell shape changes during gut morphogenesis. *Dev. Biol.* **357**, 227-234.

Roelink, H. and Nusse, R. (1991). Expression of two members of the Wnt family during mouse development–restricted temporal and spatial patterns in the developing neural tube. *Genes Dev.* **5**, 381-388.

Sato, A., Khadka, D. K., Liu, W., Bharti, R., Runnels, L. W., Dawid, I. B. and Habas, R. (2006). Profilin is an effector for Daam1 in non-canonical Wnt signaling and is required for vertebrate gastrulation. *Development* **133**, 4219-4231.

Shafer, B., Onishi, K., Lo, C., Colakoglu, G. and Zou, Y. (2011). Vangl2 promotes Wnt/planar cell polarity-like signaling by antagonizing Dvl1-mediated feedback inhibition in growth cone guidance. *Dev. Cell* **20**, 177-191.

Siedlik, M. J. and Nelson, C. M. (2015). Regulation of tissue morphodynamics: an important role for actomyosin contractility. *Curr. Opin. Genet. Dev.* **32**, 80-85.

Stanier, P., Henson, J. N., Eddleston, J., Moore, G. E. and Copp, A. J. (1995). Genetic basis of neural tube defects: the mouse gene loop-tail maps to a region of chromosome 1 syntenic with human 1q21-q23. *Genomics* **26**, 473-478.

Stumpo, D. J., Bock, C. B., Tuttle, J. S. and Blackshear, P. J. (1995). MARCKS deficiency in mice leads to abnormal brain development and perinatal death. *Proc. Natl. Acad. Sci. USA* **92**, 944-948.

Suriben, R., Kivimäe, S., Fisher, D. A. C., Moon, R. T. and Cheyette, B. N. R. (2009). Posterior malformations in Dact1 mutant mice arise through misregulated Vangl2 at the primitive streak. *Nat. Genet.* **41**, 977-985.

Sutherland, A. E. (2016). Tissue morphodynamics shaping the early mouse embryo. *Semin. Cell Dev. Biol.* **55**, 89-98.

Tada, M. and Kai, M. (2012). Planar cell polarity in coordinated and directed movements. *Curr. Top. Dev. Biol.* **101**, 77-110.

Takada, S., Stark, K. L., Shea, M. J., Vassileva, G., McMahon, J. A. and McMahon, A. P. (1994). Wnt-3a regulates somite and tailbud formation in the mouse embryo. *Genes Dev.* **8**, 174-189.

Tao, H., Suzuki, M., Kiyonari, H., Abe, T., Sasaoka, T. and Ueno, N. (2009). Mouse prickle1, the homolog of a PCP gene, is essential for epiblast apical-basal polarity. *Proc. Natl. Acad. Sci. USA* **106**, 14426-14431.

Trichas, G., Smith, A. M., White, N., Wilkins, V., Watanabe, T., Moore, A., Joyce, B., Sugnaseelan, J., Rodriguez, T. A., Kay, D. et al. (2012). Multi-cellular rosettes in the mouse visceral endoderm facilitate the ordered migration of anterior visceral endoderm cells. *PLoS Biol.* **10**, e1001256.

Tsakiridis, A., Huang, Y., Blin, G., Skylaki, S., Wymeersch, F., Osorno, R., Economou, C., Karagianni, E., Zhao, S., Lowell, S. et al. (2014). Distinct Wnt-driven primitive streak-like populations reflect in vivo lineage precursors. *Development* **141**, 1209-1221.

Tzouanacou, E., Wegener, A., Wymeersch, F. J., Wilson, V. and Nicolas, J. F. (2009). Redefining the progression of lineage segregations during mammalian embryogenesis by clonal analysis. *Dev. Cell* **17**, 365-376.

van de Ven, C., Bialecka, M., Neijts, R., Young, T., Rowland, J. E., Stringer, E. J., Van Rooijen, C., Meijlink, F., Nóvoa, A., Freund, J.-N. et al. (2011). Concerted involvement of Cdx/Hox genes and Wnt signaling in morphogenesis of the caudal neural tube and cloacal derivatives from the posterior growth zone. *Development* **138**, 3451-3462.

Vasquez, C. G., Tworoger, M. and Martin, A. C. (2014). Dynamic myosin phosphorylation regulates contractile pulses and tissue integrity during epithelial morphogenesis. *J. Cell Biol.* **206**, 435-450.

Wallingford, J. B. and Harland, R. M. (2002). Neural tube closure requires Dishevelled-dependent convergent extension of the midline. *Development* **129**, 5815-5825.

Wymeersch, F. J., Huang, Y., Blin, G., Cambray, N., Wilkie, R., Wong, F. C. K. and Wilson, V. (2016). Position-dependent plasticity of distinct progenitor types in the primitive streak. *Elife* **5**, e10042.

Xu, W., Baribault, H. and Adamson, E. D. (1998). Vinculin knockout results in heart and brain defects during embryonic development. *Development* **125**, 327-337.

Yang, W., Garrett, L., Feng, D., Elliott, G., Liu, X., Wang, N., Wong, Y. M., Choi, N. T., Yang, Y. and Gao, B. (2017). Wnt-induced Vangl2 phosphorylation is dose-dependently required for planar cell polarity in mammalian development. *Cell Res.* **27**, 1466-1484.

Ybot-Gonzalez, P. and Copp, A. J. (1999). Bending of the neural plate during mouse spinal neurulation is independent of actin microfilaments. *Dev. Dyn.* **215**, 273-283.

Ybot-Gonzalez, P., Cogram, P., Gerrelli, D. and Copp, A. J. (2002). Sonic hedgehog and the molecular regulation of mouse neural tube closure. *Development* **129**, 2507-2517.

Ybot-Gonzalez, P., Copp, A. J. and Greene, N. D. E. (2005). Expression pattern of glypican-4 suggests multiple roles during mouse development. *Dev. Dyn.* **233**, 1013-1017.

Ybot-Gonzalez, P., Gaston-Massuet, C., Girdler, G., Klingensmith, J., Arkell, R., Greene, N. D. E. and Copp, A. J. (2007a). Neural plate morphogenesis during mouse neurulation is regulated by antagonism of Bmp signalling. *Development* **134**, 3203-3211.

Ybot-Gonzalez, P., Savery, D., Gerrelli, D., Signore, M., Mitchell, C. E., Faux, C. H., Greene, N. D. E. and Copp, A. J. (2007b). Convergent extension, planar-cell-polarity signalling and initiation of mouse neural tube closure. *Development* **134**, 789-799.

Zohn, I. E., Chesnutt, C. R. and Niswander, L. (2003). Cell polarity pathways converge and extend to regulate neural tube closure. *Trends Cell Biol.* **13**, 451-454.